
Experimental study of hard marine growth effect on the hydrodynamical behaviour of a submarine cable

Marty Antoine ¹, Berhault Christian ², Damblans Guillaume ², Facq Jean-Valery ¹, Gaurier Benoit ¹, Germain Gregory ^{1,*}, Soulard T. ³, Schoefs Franck ⁴

¹ Ifremer, Marine Structure Laboratory, 150 Quai Gambetta 62200 Boulogne sur Mer, France

² France Energies Marines, 525 Avenue Alexis de Rochon, 29280 Brest, France

³ École Centrale de Nantes, 1 rue de la Noë, 44321 Nantes, France

⁴ GeM, UMR CNRS 6183, Université de Nantes, 2 rue de la Houssinière, 44322 Nantes, France

* Corresponding author : Gregory Germain, email address : gregory.germain@ifremer.fr

Abstract :

Submarine cables such as electrical umbilical power cables for floating wind turbines are subject to biofouling which can have an important effect on their dynamical behaviour under wave and current conditions by drastically increasing their size and mass. The impact of biofouling on the dynamic behaviour of an underwater power cable characterized by the hydrodynamic coefficients, such as drag and inertia coefficients, must therefore be quantified. Hence, experiments have been carried out in a flume tank to compare the dynamics of a cylinder colonized by several kinds of roughnesses. The studied roughnesses concern realistic marine growth shapes and patterns with larger and sharper edges than those classically studied, in order to be more representative of hard fouling, such as *Mytilus Edulis* encountered on the western and north coasts of France. Seven configurations are tested with relative roughness coefficient ranging from roughness to cylinder diameter ratio up to 0.136. A specificity of this work is the highly realistic representation of the marine growth colonization through 3D printing covers, defined by statistical analysis of in situ observations and measurements. Tests are carried out using current only, then in line horizontal oscillating motions only and finally the combination of both, with the intention of reproducing specific wave and current conditions suitable for offshore applications. Using current conditions, the calculated coefficients are quite similar between configurations. However, the addition of oscillating motions to simulate wave induced motions has a significant impact on calculated results. The presence of roughness leads to a particular increase of drag and inertia phenomena. The Morison method used to characterize hydrodynamic coefficients in wave conditions is discussed in this paper.

Highlights

► Hard realistic marine growth modelling. ► Colonized submarine cable hydrodynamical behaviour study under current and wave solicitation. ► Drag and inertia phenomena are governed by hard marine growth with an increase up to factor 4. ► Comparison between Morison decomposition and engineering standards.

Keywords : Dynamic cable, Cylinder, Marine growth, Roughness, Drag coefficient, Inertia coefficient

1. Introduction

Most of the Floating Wind Turbine sites are located in moderate water depths where biofouling can be observed on a major part of the water column structure with high roughness. In site submitted to current and waves, the presence of marine growth can thus have a strong impact on mooring lines responses by drastically increasing their size and mass (Ameryoun [3] or Spraul et al. [38]). Consequences of these phenomena lead to a decrease in the lifetime of the mooring lines, see Yang et al. [45]. Because biofouling is space, time and material dependent, general empirical formulas, widely used in the engineering field (see API [2] and DNV [9] standards), take into account the biofouling influence in the design process. Unfortunately, these formulations are limited due to the small number of relative roughnesses and type of geometries already studied.

Although, the flow around objects with circular cross section has received considerable attention (Sarpkaya [32], [35] [33], Morison et al. [24] and Schlichting [36]) motivated by the fundamental flow phenomena involved as well as for its relevance to engineering applications, such as mooring lines or power cables Marty et al. [19]. One of the general characteristic features is the appearance of fluctuating hydrodynamic loads which can lead to flow-induced vibrations and, if low damped, to possible structure damage. The possible influences of rough surfaces on the flow phenomena and on the surface pressures and forces acting on a circular cylinder have been investigated in many aspects already but most often with relative low roughnesses (Sarpkaya [35], Achenbach and Heinecke [1] and more recently Xiaojie et al. [44] and Vanhinsberg [42]). These studies are based on the investigation of the influence of surface roughness (characterized by its height : k) on the cross-flow around a circular cylinder (characterized by its diameter : D). All these studies agreed on the fact that the presence of roughness facilitates the appearance of a turbulent boundary layer that reduces the Reynolds number where the critical transition for the drag coefficient (C_D) occurs, from $Re = 2 \times 10^5$ with $k/D = 0$ to $Re = 4 \times 10^4$ for $k/D = 2 \times 10^{-2}$ [36]. And then, that the drag coefficient can be reduced for Reynolds numbers in the range of $4 \times 10^4 - 10^5$ in steady flow. However, in [32] and [33], Sarpkaya shows that the drag coefficient in oscillating motions can be increased by a factor 2 with the presence of roughness. Gaurier

et al. [14] studied experimentally two different kinds of large roughnesses and highlight that the associated hydrodynamic coefficients can be from 1.5 to 4 times higher than those obtained for a smooth cylinder. Teng and Nath [39] who compared experimental results of a cylinder (of diameter D) with different roughness parameters k/D from 0.02 to 0.2 showed that in presence of waves, both oscillating drag coefficient (C_d) and inertia coefficient (C_m) increase as the relative roughness increases but did not observe any dependence of the relative roughness on the C_m values for the studied conditions (waves and flow speed).

Moreover, it seems that the roughness density and more particularly the amount of surface cylinder covered by the biofouling is also a critical parameter for the calculation of the hydrodynamic coefficients, as shown in Theophanatos and Picken's works ([40], [41], [31]). According to Boukinda et al. [5], who studied the marine growth colonization in Gulf of Guinea, the thickness profiles of biofouling is non-linear with a first range between the surface and 10 – 20 m , where the marine growth increases significantly with depth, and a second one more stable between 20 m and the bottom. The average thickness calculated is around $k = 40 \text{ mm}$, which leads to a relative roughness k/D equal to 0.2 if the concerned diameter of the structure is equal to 200 mm . The studies dealing with hydrodynamic behaviours with these high values of the relative roughness are practically non-existent in the scientific literature which is generally taken up to 0.02 in Schlichting [36] and Sarpkaya [32] for example or more recently in the work of Xiaojie et al. [44]. The few studies found with large roughnesses (Teng and Nath [39] and Gaurier et al. [14]) give good trends of hydrodynamic coefficients under wave and current conditions but do not focus on the relative roughness definition which is really difficult to define in this kind of work. The first one takes the smooth cylinder diameter to calculate all parameters and the second one the external diameter. But it is shown in Ameryoun et al. [4] and Decurey et al. [8] that the definition is not that simple and has to account for some other parameters to define the right equivalent diameter. This is required to predict as accurately as possible the behaviour of offshore structures, such as mooring lines or underwater cables with a new application in a severe site (high speed and wave amplitude). Moreover, Decurey et al. [8] showed that due to internal and inter-species competition, it has been observed that mussels are often arranged in a bulbous manner. We have therefore performed a dedicated flume tank test campaign under the OMDYN2 project (*Dynamic umbilicals for floating marine renewable energies technologies - Phase 2*, [11] and Marty et al. [18] [20]). These tests are carried-out at full-scale, removing the

Reynolds similitude issue, with a highly realistic representation of mussel colonisation. Seven configurations are tested: a smooth one, two with a different homogeneous roughness and four with heterogeneous roughnesses. The purpose of the tests is firstly to quantify the impact of large roughnesses on the cylinder behaviour, and then to compare the different roughnesses depending on their constant or variable thicknesses. For this, pure current, regular forced oscillations and superimposed loadings are tested on a flume tank.

We first describe the experimental set-up including the experimental process to simulate hard fouling (mussels) concretions on a cable and the calculation method of hydrodynamic coefficients. Then, we will present the results of the experimental campaign carried out in a wave and current circulating tank. The mean drag coefficient, the vortex shedding frequency for trials under current and both inertia and drag coefficients for trials under combined current and forced motions will be compared for all configurations. A review of the Morison's equation approach for the hydrodynamic coefficient evaluation of studied structures is also presented.

2. Experimental set-up

To better understand the hydrodynamic behaviour of a submarine cable under waves and current conditions, a specific experimental assembly has been developed. The assembly is based on the use of a 6 degrees of freedom (DOF) hexapod to simulate wave effects on an instrumented cylinder (rough and smooth) submitted to a current. In this section, the assembly, the roughness modelization and the test cases are presented.

2.1. IFREMER Flume tank.

The tests are carried out in the wave and current circulating tank of IFREMER, located in Boulogne-sur-Mer (France) and presented in the figure 1.

The test section is: $18m$ long \times $4m$ wide \times $2m$ high. In this work, the three instantaneous velocity components are denoted (U, V, W) along the (X, Y, Z) directions respectively (Fig.1). Each instantaneous velocity component is separated into a mean value and a fluctuating part according to the Reynolds decomposition: $U = \overline{U} + u'$, where an overbar indicates the time average. The incoming flow $(\overline{U_\infty}, \overline{V_\infty}, \overline{W_\infty})$ is assumed to be steady and constant. By means of a grid and a honeycomb (that acts as a flow straightener) placed at the inlet of the working section, a turbulent intensity of $I = 1.5\%$ is achieved, see Gaurier et al. [15].

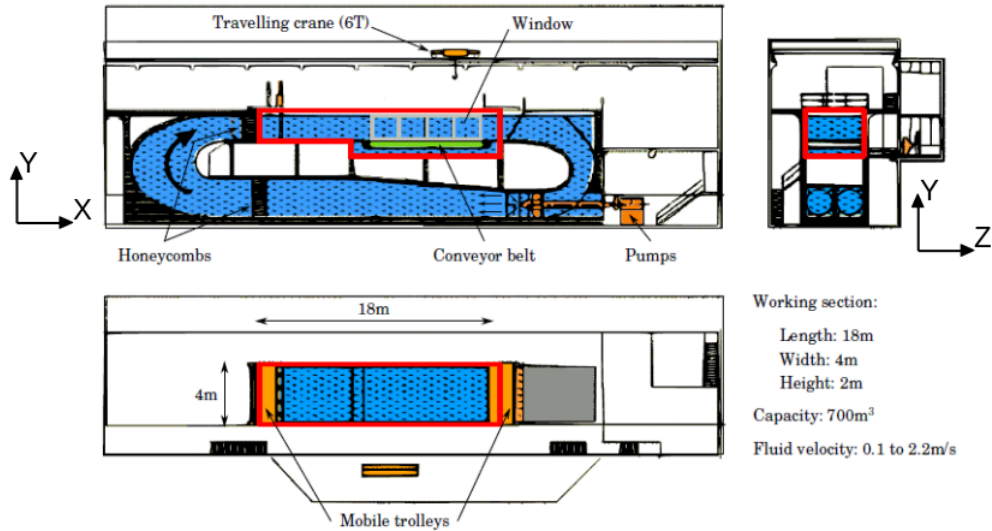


Figure 1: IFREMER Flume tank in Boulogne-sur-Mer.

2.2. Assembly and instrumentation

An overview of the global set-up is presented on the figure 2. The cylinder movements are generated using a 6-DOF hexapod on which the structure and the instrumentation are fixed. As shown on the figure 2, the cylinder is horizontally mounted so that the cylinder is located in the middle of the test section (at one meter depth). The 2 m length cylinder is perpendicular to the direction of the upstream flow. To simulate wave conditions, the hexapode moves with an oscillating and periodic motion in parallel to the flow to represent the horizontal part of the waves orbital velocity. The hexapode motions along the Ox axis are characterized by its amplitude (A_x) and its frequency (f). The axis coordinate system (X, Y, Z) is chosen so that the Ox axis is in the same direction as the current. The Oz axis is across the width of the basin and the Oy axis is vertical and oriented upwards, see the figure 3.

Two 6 components load cells, fixed at each extremity of the cylinder enable the forces applied to the cylinder to be measured. The location of these load cells is identified by their own axis systems as shown on the figure 3. The two cylindrical load cells measure the forces applied on the cylinder only, half of the total load for each cell. The cylinder is free to rotate around the z axis without any constraints along the x axis in order to build a non-hyperstatic assembly.

Concerning the measurement uncertainty analysis, forces measurements loads cells, which have a maximal loads range of $F_{x,y,z} = 1500 N$ with a measurement accuracy of 0.75 N for each load

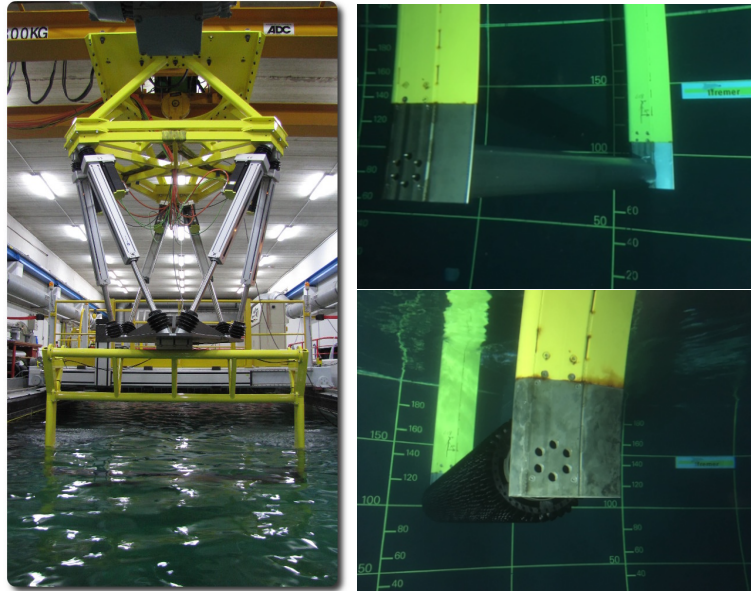


Figure 2: Presentation of the global set-up with the 6-DOF hexapod (left), the smooth cylinder (top right) and one of the rough cylinder (bottom right).

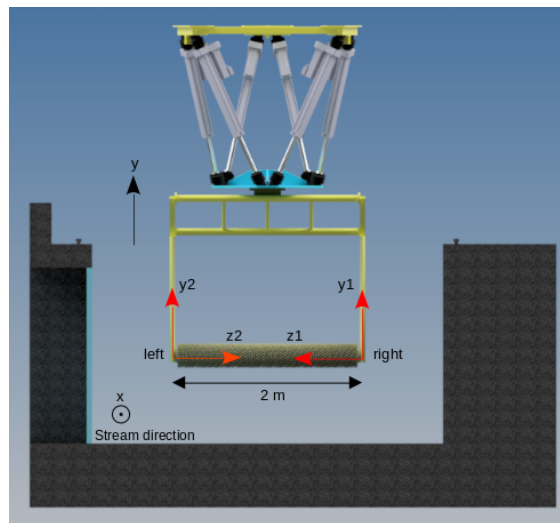


Figure 3: Axis coordinate system (X, Y, Z) used for these tests. In black, the main system. The Ox axis is common to all systems and corresponds to the main flow direction. In red, the axes of the load cells (right and left).

cell which leads to a measurement uncertainty equal to 0.05%. Drag and lift forces are calculated by adding the measurements of both cells that leads to a measurement uncertainty of 1%. From

forced motions, the precision of the hexapode is equal to 0.5 mm , in the worst-case scenario (for small motions 100 mm) it leads to a percentage of uncertainty equal to 0.5% . Finally, the turbulent intensity in the test section is equal to $I = 1.5\%$, see Gaurier et al. [15]. We therefore have a speed variation lower than 1.5% in the test section. By adding all these uncertainties we can conclude the overall measurement uncertainty is lower than 3% .

2.3. Diameters and roughness definition

One of the aims of this work is to reproduce the roughness with a highly realistic representation of mussel colonization through 3D printing covers, defined by statistical analysis of in-situ observations (Decurey et al. [8] and Spraul et al. [38]). The figure 4 represents a mooring line colonized by marine growth (*Mytilus edulis* colonisation, mussels) at different depths at the SEMREV sea test site operated by Centrale Nantes [25].

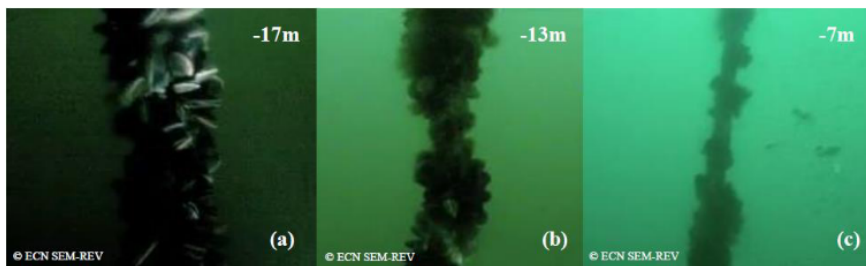


Figure 4: Illustration of *Mytilus edulis* colonisation on a small buoy mooring line, made of Deltex material at SEMREV sea test site.

From on site inspection of this cable (Schoefs et al. [37]), the size, the shape and the species distribution can be characterized. In view to create a data base that is easier to reproduce and complete in the future, it was decided to fix the roughness as a deterministic parameter and to analyse the sensitivity of the results by selecting two deterministic values. That leads to a geometrical arrangement and roughness specifications reported in the figures 6 and 7.

When mussels cluster around the rope, they do not fill all the space and create interstices full of water. In the following we consider that only the last level of mussels creates the surface roughness and the other levels create a closed and homogeneous volume due to the high concentration of mussels.

The roughness parameter (e) is defined as the ratio k/D_e , where k is the dimension of the studied roughness and D_e the equivalent diameter. In the literature, several definitions of the roughness

exist, see Achenbach and Heinecke [1] or Jusoh and Wolfram [17]. In Ameryoun et al. [4], they used a stochastic modelling of marine growth and hydrodynamic parameters to define the roughness as the ratio of the apparent height of the surface roughness (mussel length from the wider section to the external extremity, k) on the equivalent diameter of the studied configuration. Indeed, a mussel cover may be composed of several highly compact superimposed layers. As such, layers below the external one represent a thickness of closed surfaces where no fluid dynamic is permitted, with no entrapped water volume. This closed volume corresponds therefore to the difference between the whole thickness (from the internal diameter to the extremity, th) and the surface roughness (k). The figure 5 represents the different parameters for the calculation of the equivalent diameter.

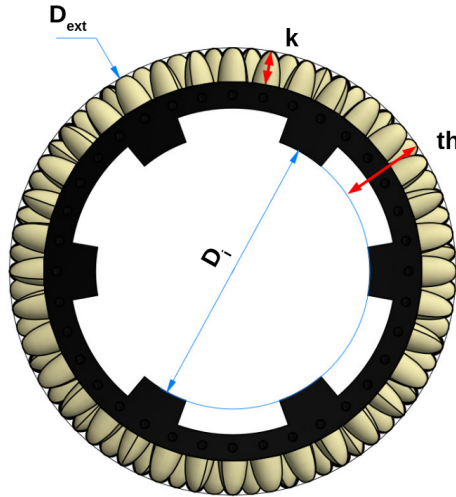


Figure 5: Definition of roughness parameters adapted to the experimental set-up.

Consequently, this thickness is assumed to be a diameter increase in a fluid dynamic point of view and thus the equivalent diameter is calculated as follow.

$$D_e = D_i + 2 \times (th - k) \quad (1)$$

Then, the thickness parameter (e) is only defined from the external layer, over a cylinder of equivalent diameter D_e . Applying the same principle on the external layer, the part below the wider section of mussel is considered to be closed. Consequently, only the mussel height upon the wider section is considered to define the roughness k , representing the surface irregularities

impacting the flow boundary layer.

To this end and by means of 3D printing, two types of mussel shape and distributions have been considered. The first one called *C1* with outside diameter (D_{ext}) equal to 260 mm with small size mussels (mussel height of 20 mm) and the second one called *C2* with outside diameter equal to 280 mm composed of larger individual mussels (mussel height of 30 mm). The design of a mussel depends on two factors, its basement shaped as an ellipse with the minor and major axes, and its height. Both configurations have an ellipse base of 16×18 mm and 20 mm tall for *C1* and 24×27 mm and 30 mm tall for *C2*. Precise dimensions are given in the figure 6.

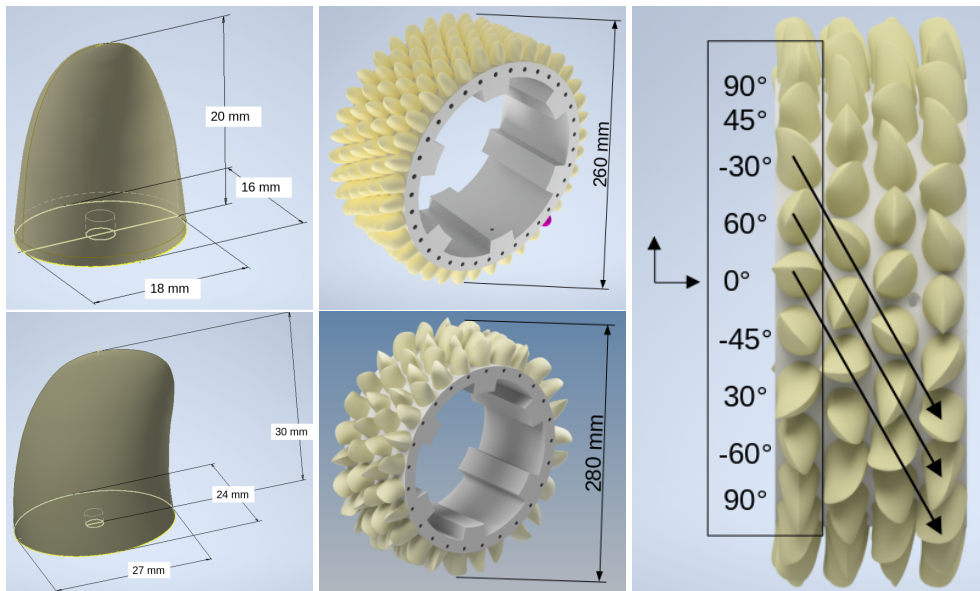


Figure 6: Mussels' dimensions for *C1* on top and *C2* at the bottom. On the right, mussels distribution around the cylinder with the *C2* shape.

For each mussel shape, the distribution around the cylinder follows the same pattern. Mussels are arranged depending on their angle between the major axis of the ellipse and the cylinder axis in such a way as to generate a stochastic distribution network as shown on the figure 6. The eight angles pattern is repeated all along the circumference of the cylinder and then reproduced along the cylinder axis with a staggered positioning, represented by the arrows on the drawing.

The experimental set-up is based on a smooth cylinder (called *S*) of diameter $D = 160$ mm, on which the roughness is superimposed in order to design a configuration with roughness, see

the figure 7. The internal diameter of the cable sample was chosen at 160 *mm* in order to be representative of 33-66kV power cables for floating wind turbines.

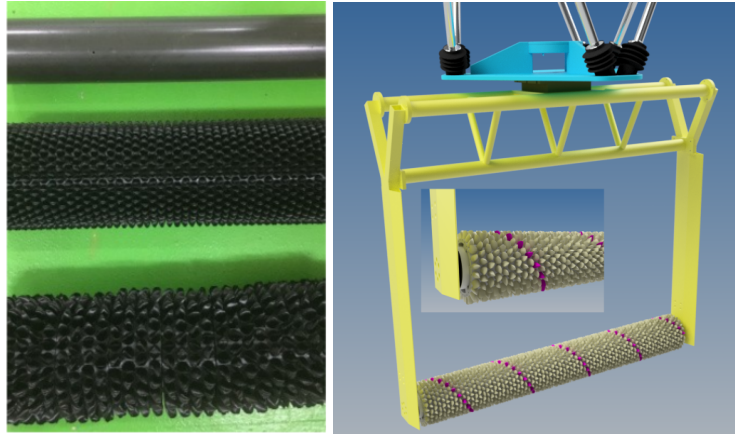


Figure 7: On the left, from the top to the bottom, cases *S*, *C1* and *C2*. On the right, *C2* roughness mounted on the cylinder.

The spatial profile of colonization by mussels has been weakly investigated in research papers, mainly because the data of the thickness was reported by divers at specific depth (maximum value of the thickness every one meter etc . . . , Picken [31]). Recently, surveys of mooring lines were analysed by means of image processing with specific algorithms (O’Byrne et al. [28], [29], [26], [27]) and the spatial profiles were reported with a high discretization in space (5 cm). A model was developed by Decurey et al. [8] who highlighted the presence of bulbs with a very complex random shape that leads to model the length and diameter of bulbs and the distance between them as random variables. The figure 8 gives an overview of the distribution of these parameters from the inspection’s records of Decurey: length of bulbs, distance between them and increase of diameter due to bulbs.

As for the roughness, our objective is to developed a test that could assess the main effect and be part of future benchmarking. The real complex and random shape is therefore simplified in view to increase the potential effect of these parameters: selection of the highest size of the bulbs (200 mm), the highest distance between bulbs and significant and representative increase of diameter (100 mm). Note that for respecting at best the meaning of equivalent diameter, the smallest distance between bulbs could be also selected. The objective here is to analyse if a modelling of loading through D_e is still reasonable in the worst geometry.

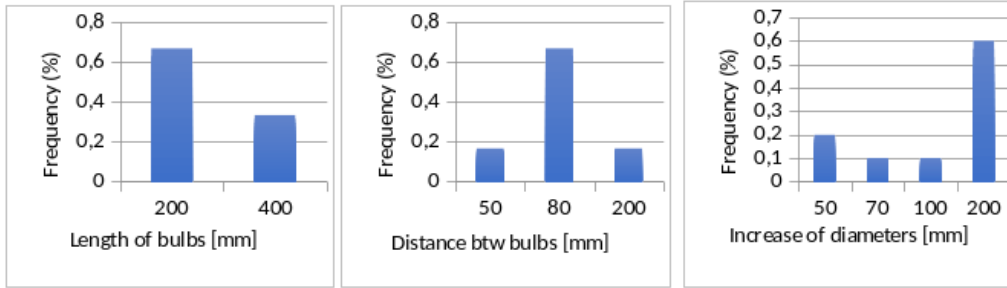


Figure 8: Distributions of length of bulbs (left), distance between bulbs (center), increase of diameter due bulbs (right).

In the following we will simulate, with different arrangements of the three kinds of cover (S , $C1$ and $C2$), a mature colonization (full coverage with mussels) and an initiation of colonization (bulbs on smooth cylinder). That leads to two "hybrid" configurations which alternate smooth and rough parts (called $C1/S$ and $C2/S$, presented in the figure 10) and two full coverages which alternate between the two roughnesses (called $C1/C2$ and $C2/C1$, see the figure 11). These configurations are representative of bulbs or lump emergence identifiable by peaks and troughs of thickness along a line, as seen on the figure 9.

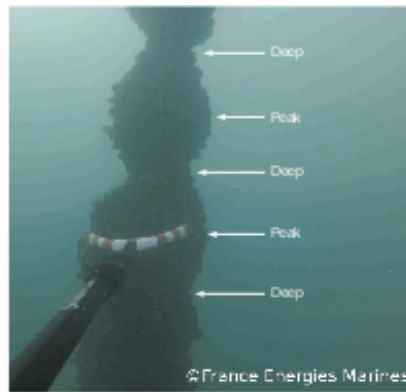


Figure 9: Bulbs of mussels defined by alternating deeps and peaks, from [8].

Thus, seven configurations are tested in this work. For the homogenous cases S , $C1$ and $C2$ the equivalent diameter is directly calculated according to equation (1). For the non-homogenous cases, the equivalent diameter (as other parameters, k and th) is the ratio between the considered roughnesses, considering that for a noted case $x1/x2$ there is 60 % of $x1$ and 40 % of $x2$, as shown in the figures 10 and 11. For instance, $De(x1/x2) = 0.6De(x1) + 0.4De(x2)$. The main

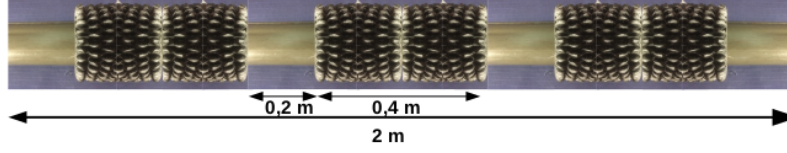


Figure 10: Assembly for the test case C1/S: roughness C1 mounted on the smooth tube of diameter $D=160\text{mm}$.

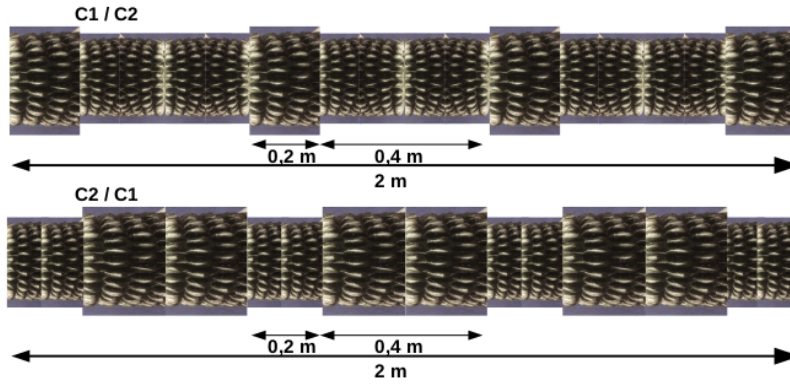


Figure 11: Assembly for the test case C1/C2 (top) and C2/C1 (bottom) mounted on the smooth cylinder.

cylinders arrangement characteristics are summarized in table 1. In this paper, all the parameters and coefficients are calculated with the equivalent diameter, D_e .

Configurations	S	C1	C2	C1/S	C2/S	C1/C2	C2/C1
D_i (mm)	160	160	160	160	160	160	160
D_{ext} (mm)	160	260	280	220	232	268	272
k (mm)	0	20	30	12	18	24	26
th (mm)	0	50	60	30	36	54	56
D_e (mm)	160	220	220	196	196	220	220
$e = k/D_e$	0	0.091	0.136	0.061	0.092	0.11	0.12
Mass system (daN)	47	105	110	85	93.5	107	108

Table 1: Synthesis of the studied roughness parameters for all configurations.

2.4. Test cases

Table 2 summarizes the main test conditions which have been imposed on the tested configurations. Tests have been carried out in current only first, then in oscillating movements without current and then finally, the combination of both. In this table, U is the current speed, A_x the motion amplitude (along x) and f the frequency of the hexapode.

	Current Alone	Motion Alone	Current + Motion
$U (m.s^{-1})$	0.25 - 1.5	-	0.25 - 1.5
Amplitude $A_x (mm)$	-	100 - 400	100 - 400
Frequency $f (Hz)$	-	0.1 - 0.75	0.1 - 0.75

Table 2: Flow and motion parameters for the tested configurations with A_x and f the motion amplitude and frequency.

All the results are presented as a function of the classical normalized numbers which are defined as follows:

- Reynolds number (Re) defined in two different ways depending on the choice of the reference speed, the flow velocity U or the oscillation speed $A_x \omega$:

$$Re = \frac{UD_e}{\nu} \quad \text{or} \quad Re = \frac{A_x \omega D_e}{\nu}, \quad \text{with } \nu \text{ the kinematic viscosity.}$$

- Keulegan-Carpenter number (KC) defined by the equation :

$$KC = 2\pi \frac{A_x}{D_e} \quad (2)$$

- The reduced speed (U_r) for current and movements cases :

$$U_r = \frac{U}{fD_e} \quad \text{with} \quad f = \frac{\omega}{2\pi} \quad (3)$$

Table 3 summarizes the value ranges of the three normalized numbers used in this study.

Configuration	S	C1-C2-C1/C2-C2/C1	C1/S-C2/S
KC	3.9 - 15.7	2.5 - 11.4	2.8 - 12.5
U_r	4.1 - 39.1	3 - 56.8	3.2 - 58
$Re/10^5$	0.4 - 2.7	0.55 - 3.8	0.5 - 3.3

Table 3: Synthesis of the normalized numbers covered for all configurations.

3. Calculation of hydrodynamic coefficients

This section presents the method used to calculate the hydrodynamic coefficients. The Morison's decomposition is first presented in detail and its accuracy is discussed after.

3.1. Formulation

In current only, the drag coefficient is calculated as follow:

$$C_D = \frac{2 \times \overline{F_D(t)}}{\rho S U^2} \quad (4)$$

with ρ the density of water ($\rho = 998 \text{ kg/m}^3$), $S = D_e \times L$ the cylinder section in front of the flow and U the current velocity. $\overline{F_D(t)}$ is the temporal mean of the drag $F_D(t)$. This coefficient is also called the *steady-flow drag coefficient*.

In the case of oscillating motions, the hexapod moves along the Ox axis, collinear with the current. The hexapod movements are oscillating with an amplitude A_x and a pulse $\omega = 2\pi f$ such as: $x(t) = A_x \cos(\omega t + \varphi_x)$. It is assumed that the answer of this excitation is a sinusoidal function as well (harmonics higher than 1 are neglected). Thus, the drag effort may be expressed as follows.

$$F_D(t) = F_m \cos(\omega t + \varphi_F) \quad (5)$$

Hence, with $\varphi = \varphi_F - \varphi_x$ it comes :

$$F_D(t) = F_m \cos(\omega t + \varphi_F + \varphi_x - \varphi_x) = F_m \cos(\omega t + \varphi_x) \cos(\varphi_F - \varphi_x) - F_m \sin(\omega t + \varphi_x) \sin(\varphi_F - \varphi_x) \quad (6)$$

$$F_D(t) = -\frac{F_m \cos(\varphi)}{A_x \omega^2} \ddot{x}(t) + \frac{F_m \sin(\varphi)}{A_x \omega} \dot{x}(t) \quad (7)$$

This equation 7 can be compared with the Morison's equation [24] :

$$F_D(t) = -\rho C_m L \frac{\pi D_e^2}{4} \ddot{x}(t) + \frac{1}{2} \rho C_d D_e L \dot{x}(t) |\dot{x}(t)| \quad (8)$$

with C_m the inertia coefficient ($C_m = C_a + 1$), with C_a the added mass coefficient) and C_d the drag coefficient. Moreover, $\sin \omega t |\sin \omega t|$ can be approximated with :

$$\sin \omega t |\sin \omega t| \approx \frac{8}{3\pi} \sin \omega t \quad (9)$$

And finally, by comparison:

$$\left\{ \begin{array}{l} C_m = \frac{F_m \cos(\varphi)}{\rho L \frac{\pi D_e^2}{4} A_x \omega^2} \\ C_d = \frac{F_m \sin(\varphi)}{\frac{4}{3\pi} \rho D_e L A_x^2 \omega^2} \end{array} \right. \quad (10)$$

For current and motion cases it is assumed that the drag effort can be divided into two parts, the mean drag part $\overline{F_D(t)}$ and the oscillating part $F_m \cos(\omega t + \varphi_F)$, such as:

$$F_D(t) = \overline{F_D(t)} + F_m \cos(\omega t + \varphi_F) \quad (11)$$

Thus, the three coefficients C_D , C_m and C_d can be calculated similarly as above (equations 4 and 10). It can be noted that these three coefficients are the same as those presented in Verley [43]. In the following, these three parameters are plotted as a function of the dimensionless numbers previously cited (R_e , KC and U_r). All the raw data of this work can be found on the data share platform SEANOE, see [20].

3.2. Accuracy of Morison's method to calculate hydrodynamic coefficients

This part focuses on the assessment of the Morison equation for the hydrodynamic coefficients calculation. This concept was widely explored (Cook and Simiu [7], Sarpkaya [34] (1981), Garrison [13] or Moe and Gudmestad [23]) and indicates that the Morison equation, used in the appropriate ranges of fluid-structure operating regimes, is a good force predictor. In [33], Sarpkaya employed the Morison equation to determine drag and inertia coefficients from an oscillating U-tube and found that, except for Keulegan-Carpenter number ranged over 20, the Morison equation represents the oscillating forces on the cylinder with accuracy.

This part of the work will discuss if the prediction of the Morison equation is appropriate here, for large hard roughnesses. We compare the drag force measured on the cylinder and noted F_m with the calculated one using Morison method (8) and noted F_c . The figures 12 and 13 represent F_m (blue) and F_c (red) for an amplitude $A_x = 200 \text{ mm}$ and different frequencies, for cases S and $C1$ respectively.

These figures highlight that the two curves match properly as long as the frequency f of the hexapode is under 0.3. Beyond this value, the Morison curves cannot reach the maximum amplitude of the measured forces. It has to be noted that a fluctuation can be observed for low forced motion frequencies in each figure. This phenomenon is caused by the cylinder vortex shedding and will be explained more in detail in the part *Effects of roughness under wave and current conditions*.

The difficulty here is to determine an accurate way to quantify the difference between the two drag forces. In [33], Sarpkaya defines a "goodness-of-fit" parameter σ given by expression (12) in which F_m represents the measured force and F_c the calculated force. Sarpkaya uses this

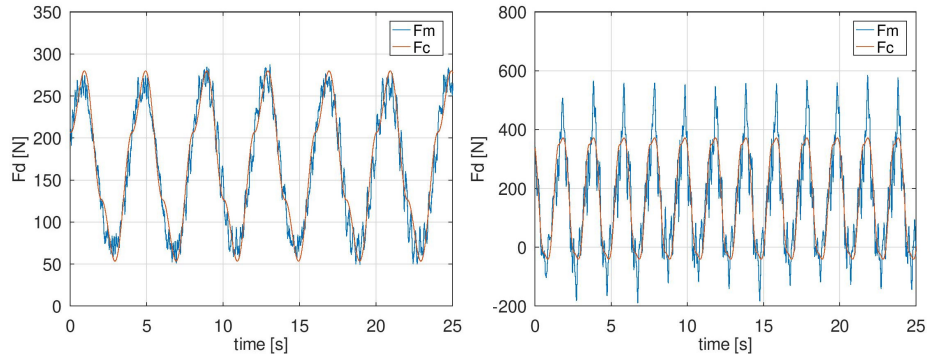


Figure 12: Drag recorded (blue) and reconstructed (red) with Morison coefficients for $A_x = 200 \text{ mm}$ and f equal to 0.25 Hz (left) 0.5 Hz (right). Case S and flow speed $U = 1 \text{ m}\cdot\text{s}^{-1}$.

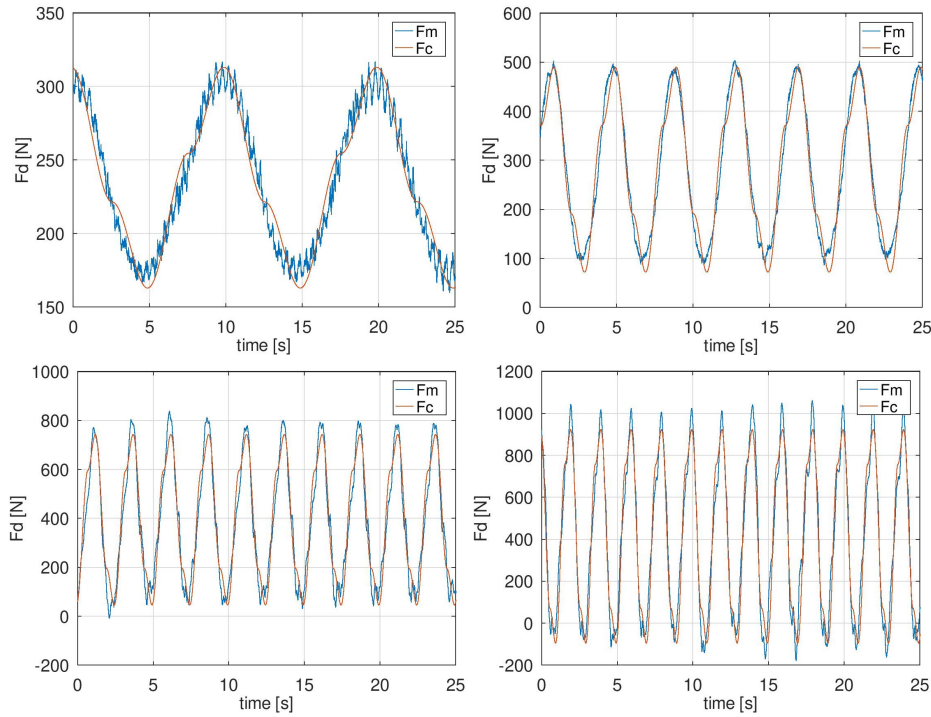


Figure 13: Drag recorded (blue) and reconstructed (red) with Morison coefficients for $A_x = 200 \text{ mm}$ and f equal to 0.1 Hz (top left) 0.25 Hz (top right) 0.4 Hz (bottom left) 0.5 Hz (bottom right). Case $C1$ and flow speed $U = 1 \text{ m}\cdot\text{s}^{-1}$.

parameter to compare the different Morison's equations, but it is quite difficult to quantify the relative gap between the measured force and the calculated one using this method.

$$\sigma = 100 * \sqrt{\frac{\frac{1}{T} \int_0^T (F_m - F_c)^2 dt}{\frac{1}{T} \int_0^T F_m^2 dt}} \quad (12)$$

The classical definition of the relative difference E_r , given in % by expression (13) can be used as long as the measured or the calculated force is not equal to zero but we see in the figures 12 and 13 that it is not always the case.

$$E_r = \left(100 * \frac{|F_m - F_c|}{|F_m|} \right) \quad (13)$$

We will then present the relative difference as the ratio between the absolute value of the difference and the mean measured force, this difference $Er1$ is given by expression (14). This method gives a good approximation but tends to minimize the relative gap compared to the classical relative difference.

$$Er1 = 100 * \frac{\overline{|F_m - F_c|}}{\overline{|F_m|}} \quad (14)$$

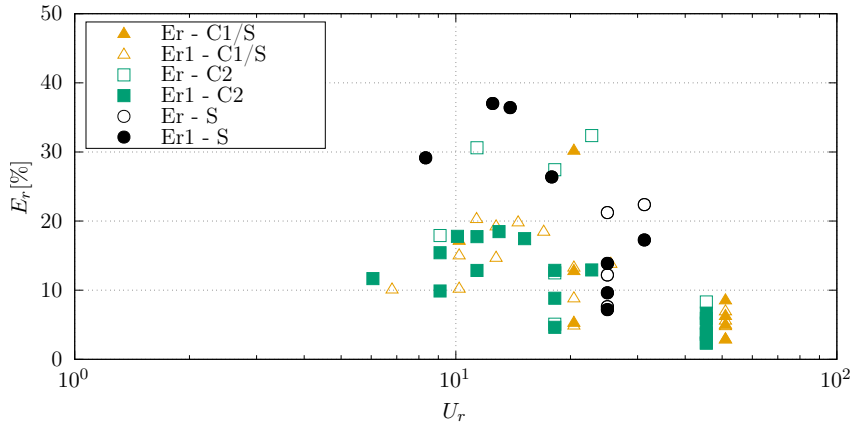


Figure 14: Relative difference for the cases S, C1 and C2 in motions and current ($U = 1 \text{ m/s}$). Er method (filled shapes) and $Er1$ method (empty shapes) see equations (13) and (14).

The figure 14 represents the relative difference using both methods of validity estimation for the cases S, C1 and C2 in oscillating motions and current with $U = 1 \text{ m/s}$. For the Er method, only cases where the measured drag force does not cross zero is represented. This graph confirms a really good agreement between F_m and F_c for low frequencies (high U_r) but can reach around 37% of relative difference for high frequencies.

A good way to study the accuracy of the Morison decomposition is to look at the difference

between the measured forces and the calculated ones by residue estimation. Residues between the real drag effort, recorded on the cylinder, and the one reconstructed by means of Morison's coefficients is calculated as follow (15):

$$R(t) = F_D(t) - \left(-\rho C_m L \frac{\pi D_e^2}{4} \ddot{x}(t) + \frac{1}{2} \rho C_d D_e L \dot{x}(t) |\dot{x}(t)| - \overline{F_D(t)} \right) \quad (15)$$

In the following, we analyse the first five harmonics of the residues, noted R_1 to R_5 , calculated by FFT means. Those residues are then non-dimensionalized by the fundamental amplitude of the recorded drag force (F_m). This ratio is expressed in % and presented in the figure 15 (for motions only cases) and 16 (for motions and current). In this way we can estimate which harmonic of the drag force is wrongly neglected by the Morison assumptions.

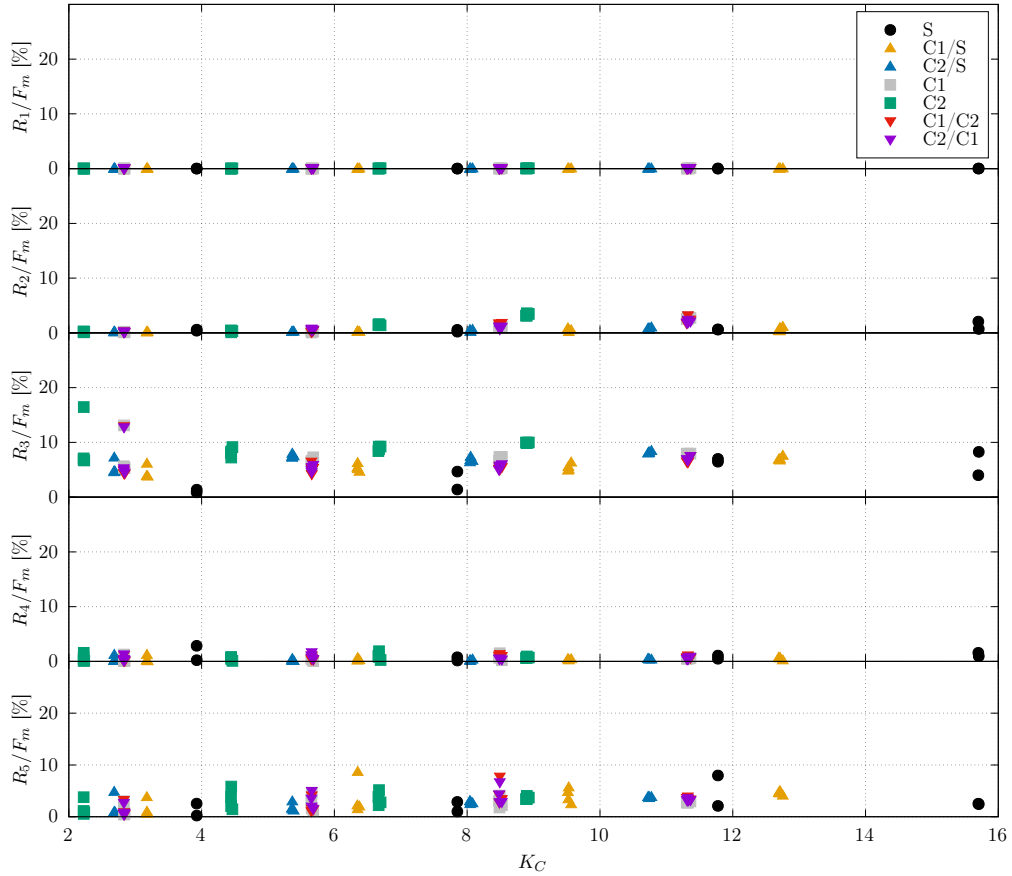


Figure 15: Residues of the first five harmonics for all cases, in motion only, as a function of KC .

Obviously, for both cases the ratio R_1/F_m is negligible because it is the assumption used for the resolution of Morison. However, in the motions case the third harmonic reaches about 10% of the F_m fundamental amplitude and in the motions and current case the second and the third harmonics reach up to 20% of the fundamental drag amplitude. The assumption of the Morison's method which states that harmonics above the fundamental one are negligible is not entirely verified.

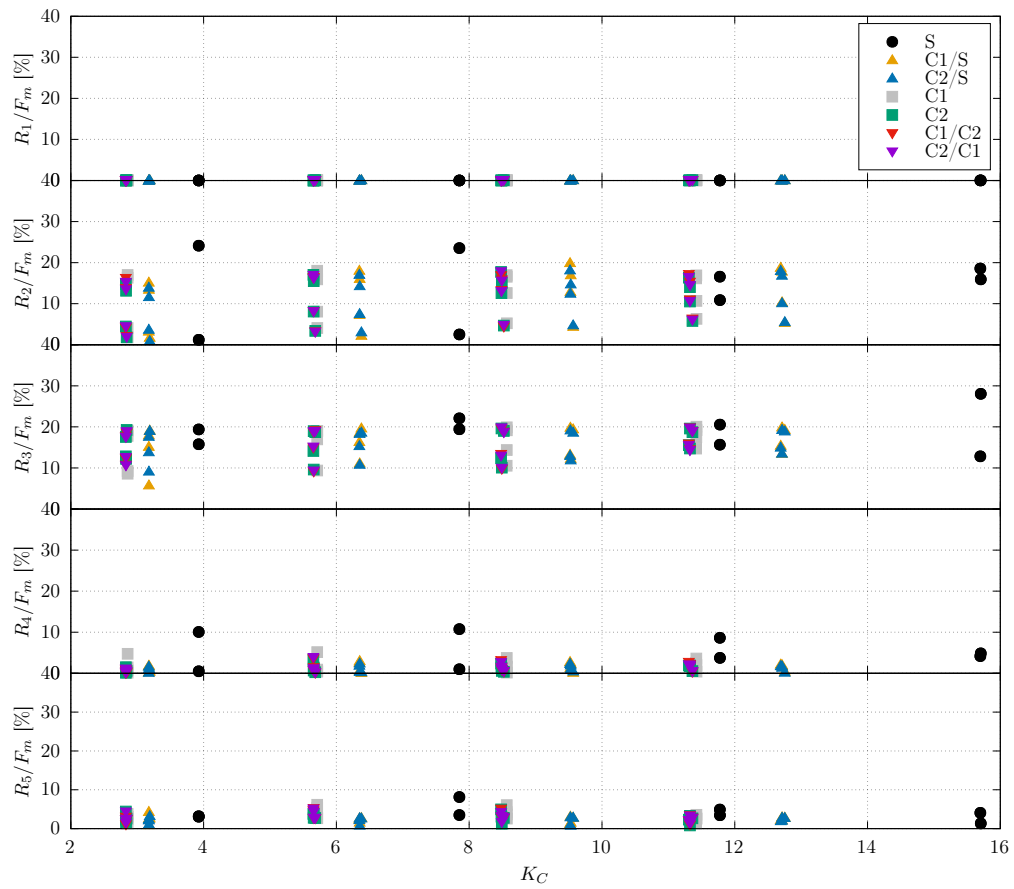


Figure 16: Residues of the first five harmonics for all cases, in motion and current, as a function of K_C . Speed current equal to $U = 1$ m/s.

The conclusion can be made in this part of the work that different methods exist to assess the validity of the Morison equation. Each method provides different information but agrees on the fact that the Morison method to calculate hydrodynamics coefficients reaches certain limits but

is overall a good force predictor for specific applications like the one presented in this paper. We can thus have a good level of confidence in the results presented in the following section.

4. Roughness effect on cylinder loads

In this section, we present the experimental results of the seven tested configurations under current conditions first, then oscillating motions only and finally the combination of both loads. For current trials, the mean drag coefficient and the vortex shedding frequency is analysed. By means of the Morison method, added mass and inertia coefficients are then investigated for oscillating tests and oscillating motions plus current tests.

4.1. Effects of roughness under current conditions

The figure 17 shows the evolution of the drag forces according to the flow velocity. In the studied flow range, the rough configurations do not show significant drag force differences (C1, C2, C1/C2, C2/C1). The curves highlight the classical evolution according to a square power law for the rough cylinders. The two partially rough configurations (C1/S and C2/S) follow the same pattern as the rough ones but slightly below, about 25% lower. This response is however different for the smooth cylinder (S) with a linear evolution until the transition obtained at a flow speed of 1.25m/s . For $U > 1.25\text{ m.s}^{-1}$, the drag is quite constant around $F_D \approx 200\text{N}$.

Note that an early-stage colonization where bulbs alternate with smooth cylinder (C1/S and C2/S) drag forces are the lowest. That indicates that in temporary conditions (early-stage colonization) the loading is the smallest. Moreover, for similar equivalent diameter (D_e) for C1, C2, C1/C2 and C2/C1, the drag forces are very close. That leads to underline the key influence of (D_e) on drag forces whatever the roughness for fully covered cylinders.

The variation of the overall mean drag coefficient C_D , the Strouhal number $S_t = \frac{f_v D_e}{U}$ (with f_v the vortex shedding frequency calculated from the lift effort recorded on the cylinder) and the r.m.s. values of the lift with Reynolds number are presented in the figure 18.

For the smooth case, the overall shape of the $C_D(Re)$ curve clearly coincides with the results presented in the literature [36]. In the subcritical Reynolds number regime a nearly constant value for C_D of about 0.9 is found. For increasing Reynolds numbers, hence by approaching the critical flow state or lower transition that starts at $Re \approx 2.1 \times 10^5$, this value gradually decreases. The minimum value of the drag coefficient of $C_D \approx 0.28$ at $Re \approx 2.7 \times 10^5$ (critical

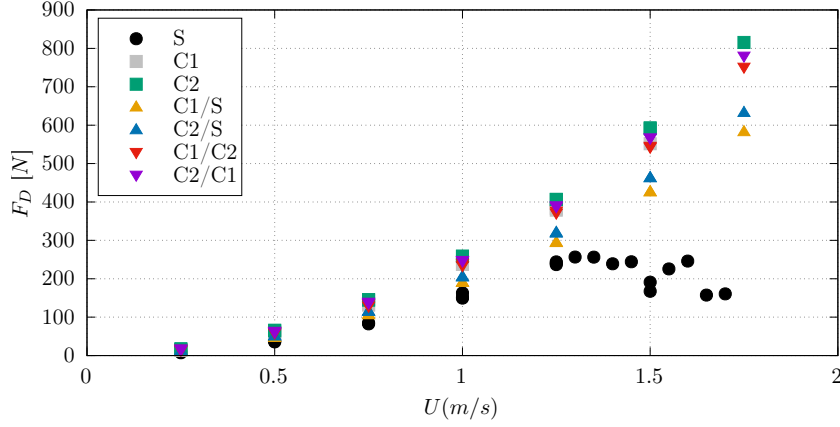


Figure 17: Drag force evolution for the seven tested cases as function of the flow speed U .

Reynolds number) marks the transition between the laminar to the turbulent flow over the cylinder. This phenomenon is well known (Verley [43], Schlichting [36]) and confirms the accuracy of the experimental set-up and of the measurements. For all rough cases (partially rough or fully rough) the transition does not occur in the flow velocity range studied. As for the drag force, three behaviours depending on cylinder roughness cover (fully rough, partially rough or totally smooth) appear. The results show that C_D increases with the size of the roughness. Fully rough configurations reach a nearly constant maximum value between 1.05 for C_1 and 1.15 for C_2 . The hybrids configurations (C_1/S and C_2/S) follow the same pattern but with lower values (about 15% lower) ranged between 0.9 for C_1/S and 1 for C_2/S .

Let us analyse the effect of the relative roughness. According to the DNV and API standards, the evolution of C_D with e follows a S shape increasing curve when $e \in [10^{-6}; 0.1]$. That is the case for C_1 , C_2/S , C_1/S with, $e(C_1/S) < e(C_1) \approx e(C_2/S)$. Results show that $C_D(C_1/S) < C_D(C_1) \approx C_D(C_2/S)$ only for $Re < 2 \times 10^5$. For larger Reynolds number $C_D(C_1) = C_D(C_2/S) + 0.1$; a uniform roughness (C_1) gives in this range a conservative value for C_D , thus for drag forces and the use of e as a key parameter is only valuable for $Re < 2 \times 10^5$. By focusing on the values, API and DNV ([2], [9]) recommends $C_D = 1$ for $e > 0.06$. For larger e , we observe that even if $e(C_1/C_2)$ and $e(C_2/C_1)$ are very close (respectively 0.11 and 0.12) $C_D(C_1/C_2) < C_D(C_2/C_1)$ with a small increase of 0.05 for $Re > 1 \times 10^5$. Parameter e looks to be valuable for ranking the C_D . Note that in standards a C_D of 1.1 is recommended for $e = 0.1$. The same order of magnitude is obtained in the present study for $C_D(C_1/C_2)$ and $C_D(C_2/C_1)$. Thus, the concept of equivalent

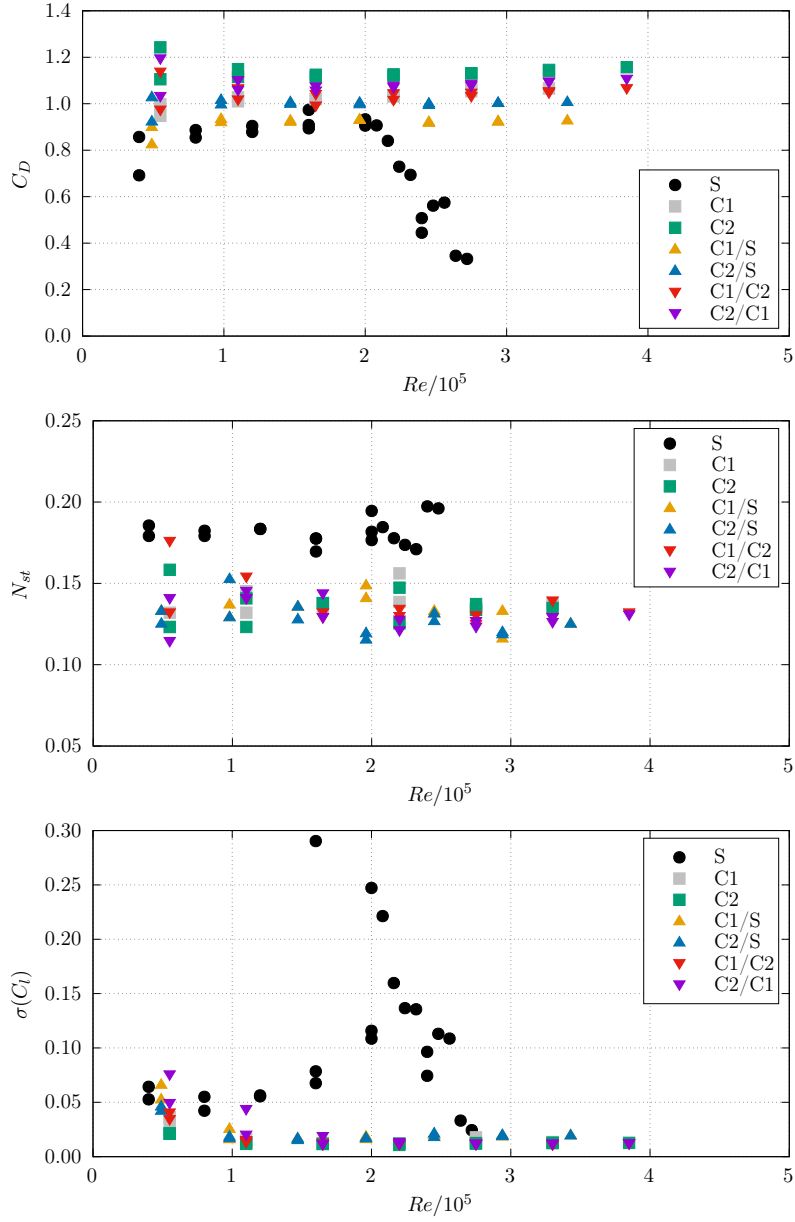


Figure 18: Distribution of C_D , N_{st} and $\sigma(C_l)$ parameters as function of the Reynolds number from direct force measurements for all the tested cases: S , $C1$, $C2$, $C1/S$, $C2/S$, $C1/C2$, $C2/C1$.

roughness seems to be valuable and at least conservative in presence of bulbs. The case $C2$ only has been discussed in (Marty et al. [21], under review).

The figure 18 (middle) presents the dependency of the Strouhal number, $S_t = \frac{f \times D_e}{U}$, on the Reynolds number. A constant value of $S_t = 0.18$ is observed in the subcritical regime for the smooth cylinder. This value is lower than the commonly used Strouhal number which is generally equal to 0.21, see Melbourne and Blackburn [22] or Vanhinsberg [42]. For all rough cylinders, the Strouhal number presents a nearly constant value of about 0.14 which is well below the smooth values. This phenomenon is well known: in Achenbach and Heinecke [1] the presence of roughness tends to decrease the Strouhal number.

The variation of the r.m.s values $\sigma(C_l)$ of the lift fluctuations with the Reynolds number is also shown in the figure 18 (bottom). A maximum value of approximately 0.3 is obtained for $R_e \approx 2 \times 10^5$ in the subcritical state due to assembly vibrations. For larger Reynolds numbers inside this flow regime a steep decrease of the r.m.s. values is observed. For all rough cases, the fluctuations are very low with : $C_l' \ll 0.05$.

These results show that the surface roughness has an important influence on the drag coefficient, the r.m.s. values of the lift fluctuations and the Strouhal number. The r.m.s. values are always lower for the rough circular cylinders. A similar trend is observed on the drag coefficient, where a difference of about 15% between cases is observed in this range ($R_e < 2 \times 10^5$).

To substantiate the fact that the presence of roughness allows to reduce physical phenomena related to vortex shedding, the Fourier transform of the lift forces ($L [N]$) as function of the frequency for each configuration and several R_e is studied in the figure 19.

The vortices are shed into the wake with different frequencies. The Fourier transform of the lift forces shows that the amplitude peaks of the vortex shedding frequencies are much higher for the smooth configuration with values of 25 N for $1.5 \leq R_e/10^5 \leq 2.5$ when it reaches only 2 N for the other rough configurations. Moreover, for the S and $C1$ configurations, we clearly see the appearance of only one peak along the frequencies evolution which is consistent with the behaviour of smooth cylinder or cylinder with small homogeneous roughness. With the other configurations which act like large and non-homogeneous roughnesses, we see the appearance of low frequency components with a reduction of the peak frequency. These large and non-homogeneous roughnesses lead to homogenize the turbulent flow around the cylinder and reduce vortex induced vibrations phenomena.

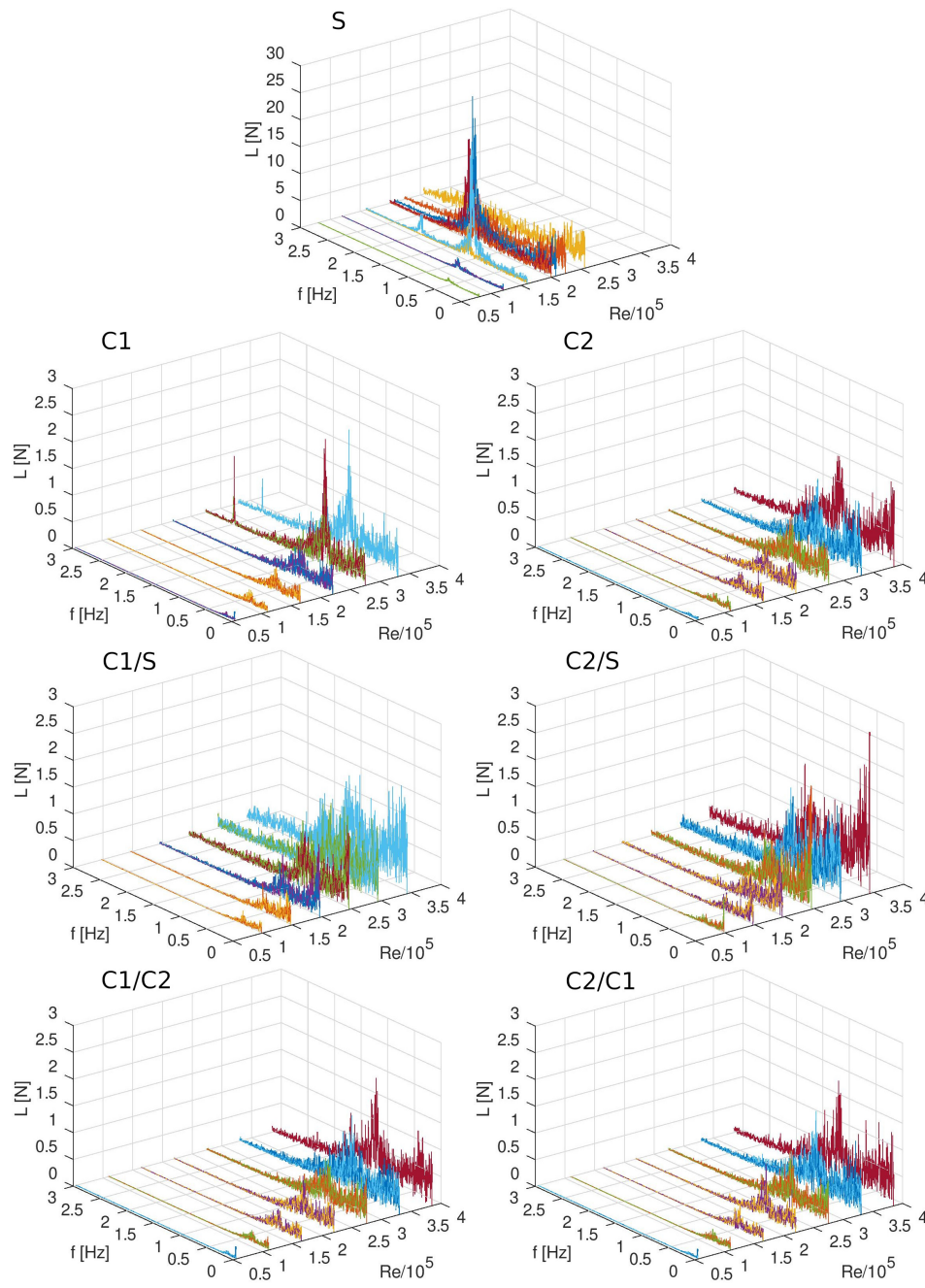


Figure 19: Fourier transform of the lift forces ($L [N]$) as function of the frequency f and Re_e for each configuration. Note that the amplitude scale of L is different for S (30 N) and other configurations (3 N).

4.2. Effects of roughness under wave conditions

For the oscillating motions test cases, the current velocity is equal to zero. The figure 20 presents the evolution of the oscillating drag coefficient C_d (top) and the inertia coefficient C_m (bottom) as a function of the Keulegan-Carpenter number KC . Several points are plotted per KC because several tests have been carried out at the same motion amplitude A_x but with different frequencies.

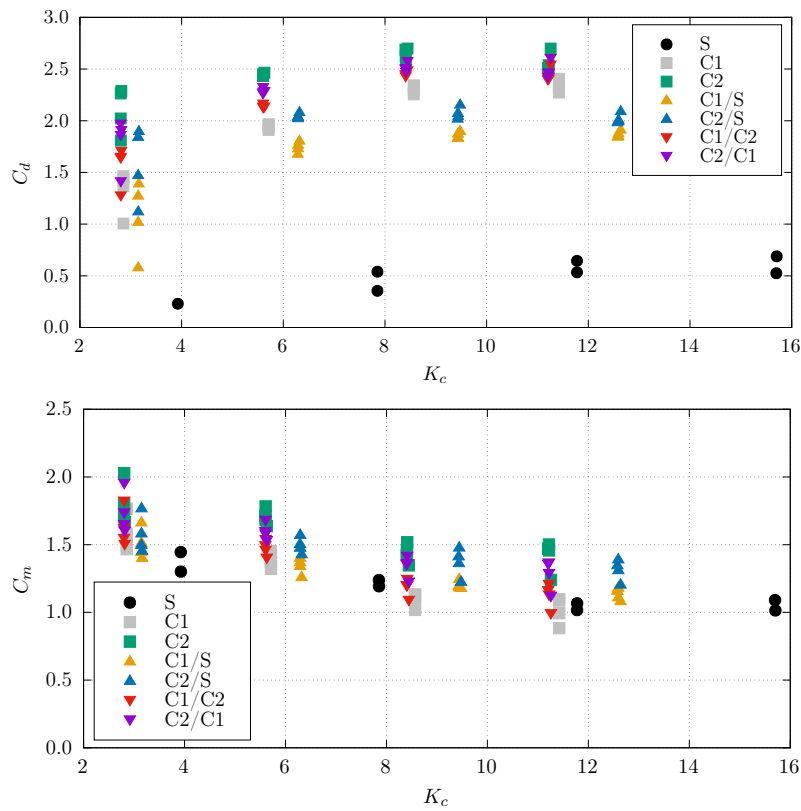


Figure 20: Oscillating drag coefficient (top) and inertia coefficient (bottom) for the seven studied configurations as function of the Keulegan-Carpenter number KC .

The results show that there is no significant difference between inertia coefficients even if the C_m of the smooth cylinder is slightly lower than the rough cases, see the figure 20 (bottom). Globally, the behaviour for the other rough or partially rough cylinders is quite the same in oscillating motions, C_2 values are just slightly higher. However, there is an important difference concerning oscillating drag coefficients between smooth, fully rough cases and partially rough

cases. The calculated coefficients are more than three times higher for fully rough cases ($C1$, $C2$, $C1/C2$ and $C2/C1$) compared to the smooth case, with $C_d \approx 2.5$ for $KC > 6$ for the rough cases and $C_d \approx 0.5$ for $KC \leq 16$ for the smooth cylinder. As is the case for current only, the C_d graph highlights three different behaviours between the fully rough cases, the partially rough cases and the smooth case. Values for partially rough cases follow the same pattern as fully rough cases but are ranged below, about 25%.

These results highlight the fact that the behaviour of the rough cylinders is mainly governed by the flow and not by their motions (see Chaplin and King [6]), contrary to the smooth cylinder for which its behaviour is mainly governed by its motions.

4.3. *Effects of roughness under wave and current conditions*

This section presents results concerning current and oscillating motions tested cases. The same coefficients previously studied for the two other test conditions are calculated, which are the mean drag coefficient C_D , the oscillating drag coefficient C_d and the inertia coefficient C_m . These coefficients are at first presented configuration by configuration as a function of U_r on the figure 21 (only S , $C2$ and $C2/S$ for reasons of clarity). From these results, we can see that the coefficients for both rough cases are not significantly different, particularly for the mean and oscillating drag which are very close. The inertia coefficients for the rough cases present less dispersion than for the smooth cylinder, therefore its evolution does not depend on the oscillating frequencies. For $U_r < 10$, the mean drag coefficients are twice as high for the rough cases as for the smooth one. These results confirm that the behaviour of the rough cylinders is mainly governed by the flow and not by their motions, contrary to the smooth cylinder for which its behaviour is mainly governed by its motions.

The figure 22 presents each coefficient for the seven studied configurations. In order to compare the behaviour of each configuration with clarity, the current velocity is fixed at 1 m.s^{-1} . These coefficients are represented as a function of the reduced speed for all the motion amplitudes in order to study the amplitude and the frequency parameters effects at the same time.

The results present several and opposite behaviours of the coefficients evolution. First of all, the inertia coefficient (C_m) tends to be similar for each configuration. The higher the frequency (small U_r), the lower the coefficient. Moreover, we can conclude that the motion amplitude has no impact on the evolution of the inertia coefficient. Indeed, it is obvious here that the amplitude curves are evolving jointly.

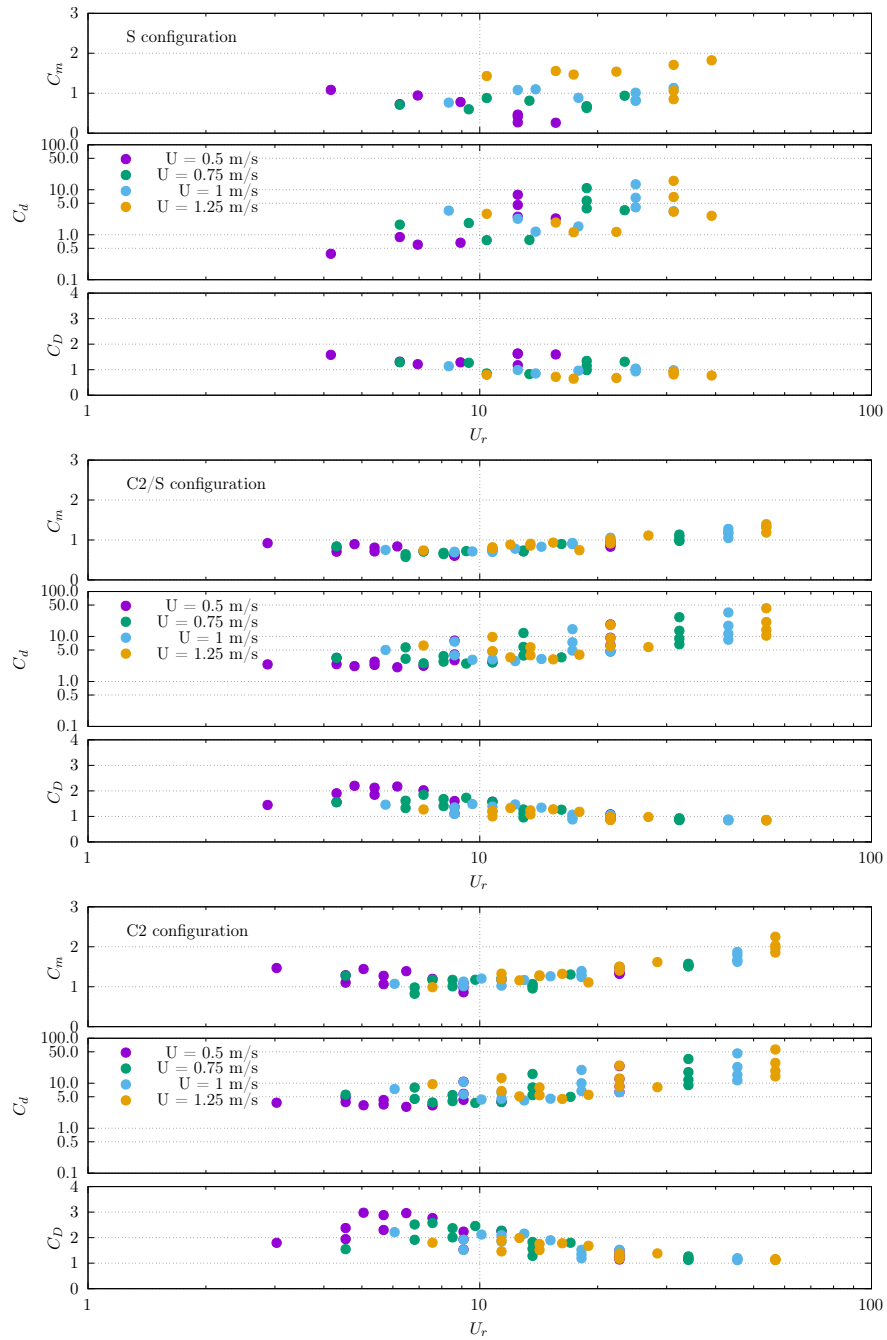


Figure 21: Inertia coefficient C_m , oscillating drag coefficient C_d and mean drag coefficient C_D as function of the reduce speed U_r for the S (top), C2/S (middle) and C2 (bottom) cases.

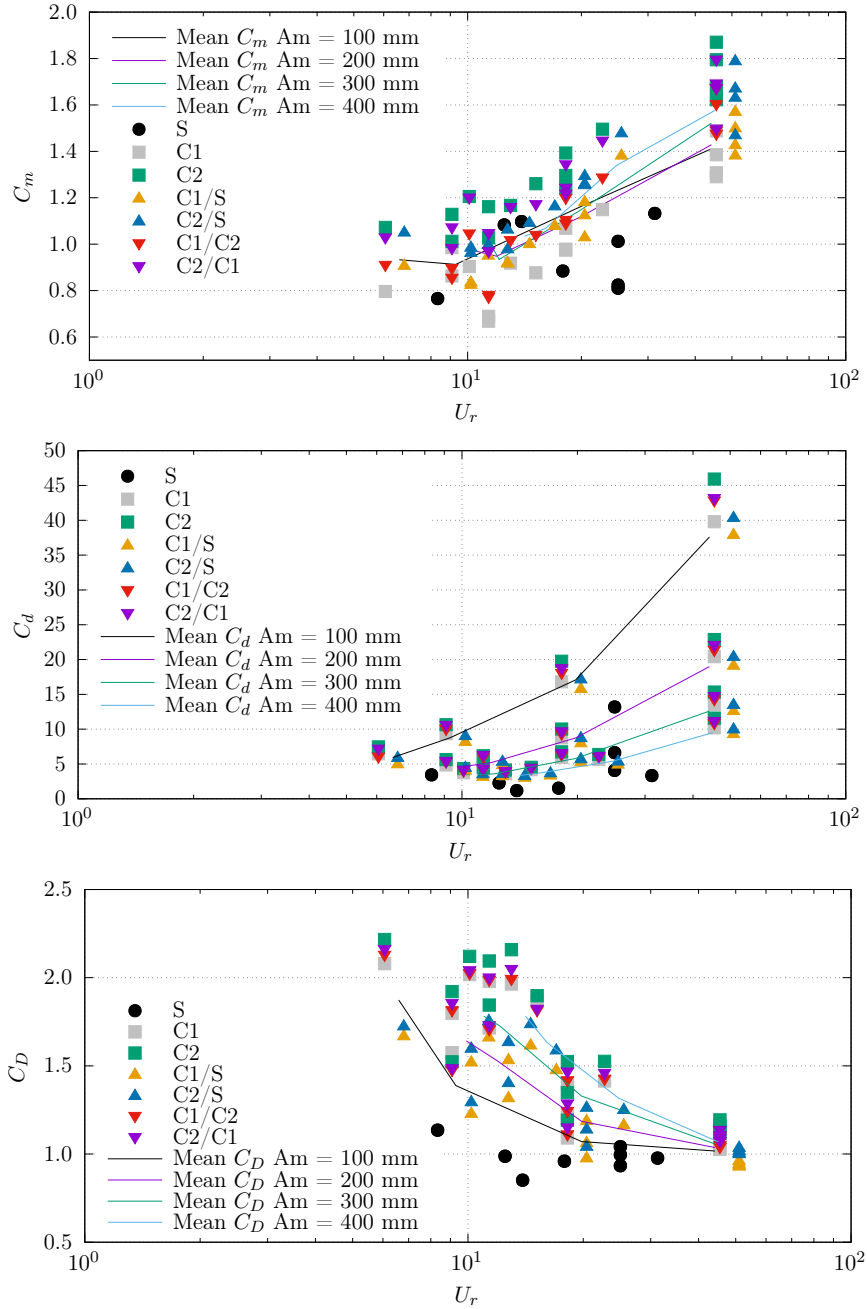


Figure 22: Inertia coefficient C_m , oscillating drag coefficient C_d and mean drag coefficient C_D as function of the reduce speed U_r for the tested configurations. Compared to the mean values of each amplitude. For a current speed $U = 1$ m/s.

Regarding drag coefficients (C_d and C_D), their behaviours are totally the opposite. The value of the coefficient C_d increases with the reduced velocity U_r . Moreover, for a fixed frequency (or U_r fixed) the amplitude parameter has a big impact and the value of the coefficient increases when the amplitude A_m decreases. The exact opposite phenomenon occurs concerning the mean drag coefficient C_D , with the value of the coefficient decreasing when the amplitude A_m increases.

Finally, as for the previous case, there is an important difference concerning oscillating drag coefficients and mean drag coefficient between smooth and rough cylinders. The calculated coefficients are much higher for fully rough cases $C1$, $C2$, $C1/C2$ and $C2/C1$ compared to the smooth case for which there is no dependency on the motion amplitude and frequency. As in the two other cases studied, coefficients calculated for the partially rough configurations ($C1/S$ and $C2/S$) follow the same pattern with fully rough cases but with slightly smaller values, between 10% and 20% lower. A strong dependency on the amplitude of the drag coefficients at fixed frequency for the rough cases is clearly highlighted here.

Concerning the measured data fluctuation which has been highlighted in the part 3.2 for low forced motion frequencies, this fluctuation (equal to 2.4 Hz) may come from the cylinder vortex shedding. Indeed, for low forced motion frequency (here $f=0.1$ Hz), and therefore low oscillating speed, the system behaves as if it was in pure current. In this example, the oscillating speed ($U_{osc} = A_x \times \omega = A_x \times 2 \times \pi \times f = 0.1256$ m/s) combined with the current speed ($U = 1$ m/s) can lead to a cross-flow speed equal to 1.1256 m/s which is equivalent to a Reynolds number $Re \sim 2.5 \times 10^5$ for the $C1$ case. When we look at the frequency behaviour of the case $C1$ in pure current (figure 19 case $C1$) we see on the frequency spectrum (for $Re \sim 2.5 \times 10^5$) a first peak corresponding to the fundamental frequency and a second peak at exactly $f = 2.4$ Hz which can be the reason why the measured data fluctuate only in this case. Moreover, the same exercise with the same conclusion can be made for the case S . Thus, the fluctuating frequency showed on the temporal signal (figure 12 and 13) for oscillating and current case (only for low oscillating speed) is contained on the frequency spectrum of the current only case, which shows that these two configurations are related.

Nevertheless, this phenomenon does not change anything in the calculation of the hydrodynamic coefficients because the Morison method assumes the answer of the drag force to a sinusoidal excitation is a sinusoidal function at the same frequency for which harmonics larger than 1 are neglected.

5. Discussion

The present measurements constitute the first experimental campaign with different large and highly realistic marine growth roughnesses under wave and current conditions. It takes into account the heterogeneity of the marine growth distribution on submarine cable such as submarine power cables. Assumptions regarding the assessment of the marine growth and the roughness parameters are numerous and debatable. As suggested by the standard certifications (American Petroleum Institute (API) [2] or Det Norske Veritas (DNV) [9]), we defined the roughness by the overlay of a closed volume and an opened one corresponding to the surface roughness. The first closed layer increasing the diameter in a fluid dynamic point of view enables us to define an equivalent diameter (D_e). Then the external layer, corresponding to the apparent height of the surface roughness and defining the studied roughness (k). These options appeared to be the most appropriate for this work, but other choices are possible such as opting to define the reference diameter as the external one.

From all tests carried out in this work, the presence of realistic roughness has a significant influence on the hydrodynamic behaviour of a cylinder subject to current and wave conditions. The study of the drag coefficients (C_D and C_d) as a function of the current and wave parameters highlights three behaviours according to the type of roughness studied. The three categories concerned are the smooth cylinder (S), the partially rough ones ($C1/S$ and $C2/S$) and the fully rough cylinders ($C1$, $C2$, $C1/C2$ and $C2/C1$). The more the amount of surface cylinder is covered by the biofouling, the more the drag coefficient increases. The drag coefficients calculated for fully rough cylinders can be four times higher than for the smooth case. The fully rough cylinders drag coefficients and partially rough ones follow globally the same behaviour but the partially rough calculated values are each time below the full rough ones ($\sim 20\%$).

From vortex shedding frequency analysis, the presence of roughness tends to reduce the excitation phenomena in frequency and amplitude. The amplitude peaks of the vortex shedding frequencies are much higher for the smooth configuration than the rough one with a difference of about 90%. The r.m.s. values are always lower for the rough circular cylinders. The overall behaviours between rough configurations seem similar for fully rough and partially rough cylinders concerning the frequency analysis (Fourier transform).

For the oscillating cases, the results do not highlight a significant difference for the inertia coefficients (C_m) between all configurations. The presence of roughness increases the calculated

values of C_m but similarly for all rough configurations. These conclusions are similar to the work of Teng and Nath [39], who compared experimental results of a cylinder with different large roughnesses. They show that C_d and C_m increases as the relative roughness increases but do not observe any dependence of the C_m values on the relative roughness for the studied conditions (waves and flow speed).

The oscillating and current cases highlight a strong dependency on the amplitude of the drag coefficients at fixed frequency for the rough cases while they are stable in static. This shows that the commonly used approach ([2], [9]) of $C_d = \psi(KC).C_D(Re)$ is not legitimate. Moreover, while Morison's linearisation for static drag force is justified, it means that it is not for oscillating cases, the KC defined only with the amplitude is not representative of the flow variety. This number should also depend on the frequency or the reduced speed. These results highlight the fact that the behaviour of the rough cylinders is mainly governed by the flow and not by their motions, contrary to the smooth cylinder for which its behaviour is mainly governed by its motions.

To illustrate this point, the figure 23 presents a comparison between the calculated C_D from the experimental campaign (filled forms) and DNV's predictions ([10], empty forms) for the configurations S , $C1$ and $C2$ in current only case. The predicted coefficients (called $C1 - DNV$ and $C2 - DNV$) are calculated from the S coefficients using the expression (16). With D_i the internal diameter and k the studied roughness. We keep the equivalent diameter D_e of each configuration to calculate the associated Reynolds numbers.

$$C_{D,growth} = C_{D,smooth} \times \frac{D_i + 2 \times k}{D_i} \quad (16)$$

Only the permanent part of the drag coefficients evolution, corresponding to the subcritical flow of the S configuration, is presented in the graph. Indeed, on the covered range of Reynolds numbers studied here, the evolution of the drag coefficient in the rough cases ($C1$ and $C2$) stays permanent, see part 4.1. Results shows that the predicted coefficients are close to the experimentally measured ones, therefore the DNV's method is a good way to predict rough behaviour in the subcritical regime and current only.

The same exercise is reproduced in the oscillating case (without current) and presented in the figure 24 for the oscillating drag coefficients C_d and the inertia coefficients C_m . The prediction methods are different from the current case. The DNV's coefficients in oscillating motions are calculated from the static ones measured in current only (C_D) using a correction function. For

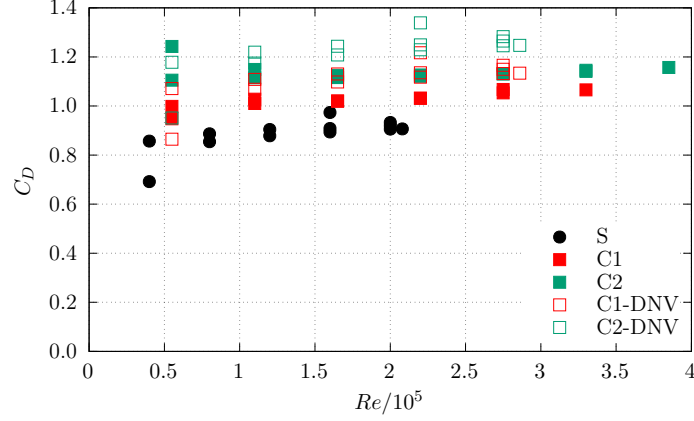


Figure 23: Comparison between calculated C_D from the experimental campaign and DNV's predictions for current only.

the drag coefficient, the correction function $\psi(KC)$ is given by the relation (17) for $2 < KC < 12$.

$$C_d = C_D \times \left[1.5 - 0.024 \left(\frac{12}{C_D} - 10 \right) + 0.1(KC - 12) \right] \quad (17)$$

The C_m coefficients, according to the DNV's rules, are given by the relation (18) for $KC > 3$.

$$C_m = \max \left\{ \begin{array}{l} 2 - 0.044(KC - 3) \\ 1.6 - (C_D - 0.65) \end{array} \right\} \quad (18)$$

The aim of these formulas is to determine the oscillating drag and inertia coefficients from the mean drag coefficient calculated in current only for the equivalent configuration. For example, the mean drag coefficient of C2 for current only case is equal to 1.14, this value is then integrated in (17) to calculate the oscillating one. Thus, the figure 24 represents the comparison between the predicted oscillating drag coefficient C_d (top) and the inertia coefficient C_m (bottom) in an oscillating case with its experimental equivalents.

These results show a good agreement between the measured values and the calculated ones for the inertia part (C_m). Indeed, as predicted, the overall evolution of this coefficient does not depend on the roughness cover and decreases with the KC number. As shown on the graph, the three DNV curves are superimposed. This is due to the fact that the C_m prediction given by the relation (18) only depends on the KC number in our case because the maximum is always given by the relation $2 - 0.044(KC - 3)$. For the oscillating drag coefficients, the difference between the DNV's prediction coefficients and the measured ones increases with the roughness. The estimation is

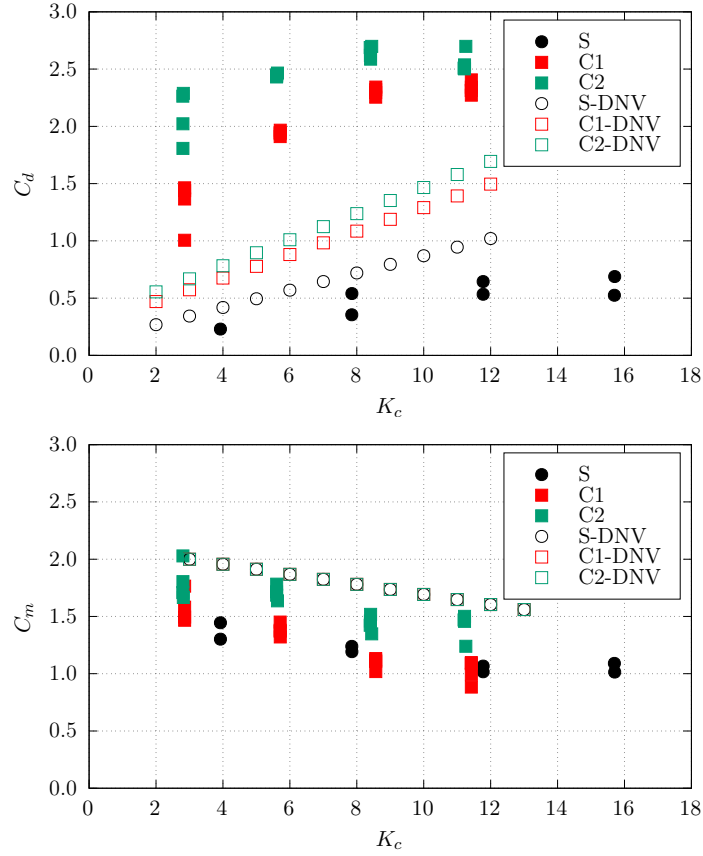


Figure 24: Comparison between the predicted C_d (top) and the inertia coefficient in oscillating case (C_m , bottom) with its experimental equivalents.

fairly good concerning the smooth case but for the rough cases, results show a large gap between the predicted and the measured coefficients even if the trend seems good.

The differences highlighted in these comparisons may come from various origins. First of all, the sizes and shapes of the studied roughnesses are higher in this study ($\sim 10^{-1} m$) than in the literature or standards ($\sim 10^{-4}/10^{-2} m$). As seen previously, this parameter has a stronger impact on the drag phenomena than on the inertia ones, therefore it makes sense that bigger differences are highlighted on the drag coefficients than on the inertia coefficients. And last, but not least, all references on which these standards are made are based on the assumption that the cylinder diameter is negligible compared to its length ($D/L \ll 1$) and consider the study of a cylinder with no side effects, which is not the case here. Several studies show that these parameters has a

significant impact on the mean drag coefficient (Okamoto and Yagita [30], Gao et al. [12] based on Wieselsberger's results) which is reduced when the D/L ratio increases, as well as standards (DNV or API) which recommend the use of a reduction factor (κ) for a cylinder of finite length. Okamoto and Yagita [30], who studied a circular cylinder of finite length placed normal to a plane surface, compare the drag coefficient measured near the plane surface with the one measured near the free-end cylinder and show that the drag coefficient is higher when the sensor is located near the plane surface where there is no side effect. These facts are some reasons why the mean drag coefficients calculated from the experimental campaign in current tests (~ 0.9 in subcritical flow, see the figure 23) are lower than values found in the literature for a same test campaign at a same flow regime (~ 1.2). Furthermore, if we correct this theoretical drag coefficient with the reduction factor recommended by standards for finite length member and corresponding to the ratio used in this campaign ($L/D = 12.5$ for smooth case) which is equal to 0.7, we find approximately the calculated mean drag coefficients of this study ($1.2 \times 0.7 = 0.84$). Moreover, this three-dimensional aspect highlights that in this work, inertia related phenomena and calculated drag coefficients are always slightly underestimated compared to an infinite cylinder where the three-dimensional aspect is negligible.

Finally, the different ways to assess the validity of the Morison equation presented in this work show the limits of this methodology for high roughnesses at high waves and current conditions. Nevertheless, the Morison method remains a good force predictor depending on the use made of it, especially for low wave frequencies.

Moreover, the behaviour of the cable is different if we are in presence of hard or soft marine growth. In Henry et al. [16] they compared hard marine growth (sand roughness) with soft marine growth (artificial fur) and showed significant differences between these two types of biofouling.

It is important to note that the species that form marine growth are diverse and show a wide range of different life traits (i.e. they are variable in length/height, in flexibility/stiffness, in gregariousness). The mussel (*Mytilus edulis* type) has been chosen for several reasons :

- this species has often been observed at offshore sites where their development may be extensive in thickness,
- its shell sharp edges are supposed to significantly influence local flow,

- it is a cosmopolitan species developing in all the oceans of the world.

Investigations should be carried out considering other biofouling species. To proceed, marine growth species have to be classified by categories according to their stiffness, mass ratio (against seawater) and mean height.

Some considerations can be shared on a few group of species, which are commonly found in biofouling assemblages. In contrary to mussels, barnacles do not grow in several superimposed layers and their height is generally lower. For that reason, the need to use an external diameter so including an homogeneous increase in diameter is anecdotal. In addition, barnacles are mainly present at early biocolonisation stages, so close to the first layer and despite highly rough wall-plates, the geometry is more axisymmetric and does not show pronounced sharp edges of lifting profile nature such as mussel. For that reason, expected hydrodynamic effects of barnacles are probably very closed to effects already measured in previous studies/existing literature, both in term of roughness ratio k/D and tested roughness texture. Small algae show a very low mass ratio, so their impact is more expected on the drag but the high flexibility may change the trend. Sea sponges are an intermediate category with a mass ratio close to 1 (almost full of water) and are relatively flexible. This kind of biofouling should be studied in detail. Large seaweeds like laminaria may be 20 times longer than a cable diameter (i.e. up to 4m long compared to 20cm cable diameter) and are highly flexible organisms. There is therefore no meaning to assume that biocolonization by laminaria seaweeds shows roughness and the use of standard Morison formulations is probably inappropriate in this case. Highly coupled fluid/structure approach dedicated to answer this question should be set up in order to model this specific behaviour.

6. Conclusion and Perspectives

The aim of this work was to compare realistic roughnesses with high dimensions and categorized into several groups, such as homogeneous or non-homogeneous roughnesses along the cylinder. This phenomenon has therefore been partially investigated in this work for a specific kind of biofouling, hard and large marine growth.

From a dynamical point of view, drag coefficients are always lower in the case of a non-homogeneous cover than for homogeneous ones. This point is important for the engineering design phase of submarine cables. The presence of roughness also affects the inertia coefficient compared to a smooth case, but the trends of the inertia phenomena do not depend on the rough-

ness distribution. The velocity components therefore appear to be the most constraining part in the design stage of a submarine cable.

The results presented in this work lead to a better understanding of the impact of marine growth on the hydrodynamic behaviour of a submarine cable under wave and current conditions. The evolution of the hydrodynamic coefficients as a function of the different wave and current parameters highlights a strong dependency between hydrodynamic loads and roughnesses, especially for the velocity part. Thus, the increased diameter by the marine growth thickness seems to be a preponderant factor in the overall evolution of coefficients compared to the mass and the added mass increase of the structure. By comparing hydrodynamic loads on cylinders with similar rough distributions but different density, and therefore masses, we could confirm or cancel this assumption.

More globally, it may be interesting to perform systematic tests in order to be able to specify accurate recommendations for in-situ measurements. Indeed, the present study shows that the most influencing parameter of a hard fouling cover is the surface protuberance field seen as a roughness, and therefore its equivalent diameter D_e . Unfortunately, this parameter is the most difficult to quantify at sea, so requiring a millimetric accuracy on mobile components in an environment of moderate to high turbidity. It becomes important to fix the necessary level of accuracy of such measures based on large basin tests / numerical campaigns involving high fidelity fouling covers:

- The different roughness configurations (partial, total, roughnesses mix) show weak differences and their effects seem to be linearly superposed for non-homogeneous cases. It will be interesting to identify a possible threshold from which the length of a bulbous area vs length of a transition area induces a linear superposition of local flow as per illustrated here through the frequency analysis. This may help to anticipate brutal change in a hydromechanical response ;
- Recommendations on the best statistical approach for a representative description of individual protuberance height distribution may help greatly. This analysis may be done through tests involving heterogeneous individual height in focusing on a neighbouring field (area of wake sheltering smaller specimens...)

Acknowledgment

This work benefits from funding from France Energies Marines as well as the French National Research Agency under the Investments for the Future program bearing the reference ANR-10-IEED-0006-28. This project was partly financially supported by the European Union (FEDER), the French government, IFREMER and the region Hauts-de-France in the framework of the project CPER 2015-2020 MARCO.

References

- [1] Achenbach, E. and Heinecke, E. (1981). On vortex shedding from smooth and rough cylinders in the range of Reynolds numbers $6e3$ to $5e6$. *Journal of fluid mechanics*, 109:239–251.
- [2] American Petroleum Institute (API) (2000). Planning, Designing and Constructing Fixed Offshore Platforms - Working Stress Design. API Recommended Practice 2A-WSD (RP 2A-WSD) twenty-first edition, American Petroleum Institute (API).
- [3] Ameryoun, H. (2015). *Probabilistic modeling of wave actions on jacket type offshore wind turbines in presence of marine growth*. PhD thesis, University of Nantes.
- [4] Ameryoun, H., Schoefs, F., Barrillé, L., and Thomas, Y. (2019). Stochastic modeling of forces on Jacket-Type offshore structures colonized by marine growth. *Journal of Marine Science and Engineering*, 7(5):158.
- [5] Boukinda, M. L., Schoefs, F., QuiniouRamus, V., Birades, M., and Garretta, R. (2007). Marine growth colonization process in guinea gulf: Data analysis. *Journal of Offshore Mechanics and Arctic Engineering*, 129(2):97–106.
- [6] Chaplin, J. R. and King, R. (2018). Laboratory measurements of the vortex-induced vibrations of an untensioned catenary riser with high curvature. *Journal of Fluids and Structures*, 79:26–38.
- [7] Cook, G. R. and Simiu, E. (1989). Hydrodynamic forces on vertical cylinders and the lighthill correction. *Ocean Engineering*, 16(4):355–372.
- [8] Decurey, B., Schoefs, F., Barillé, A. L., and Soulard, T. (2020). Model of bio-colonisation on mooring lines: Updating strategy based on a static qualifying sea state for floating wind turbines. *J. Mar. Sci. Eng.*, 8(2):108.
- [9] Det Norske Veritas (DNV) (2010). Offshore Standard Position mooring. <https://rules.dnvgl.com/docs/pdf/dnv/codes/docs/2010-10/rp-c205.pdf>, Det Norske Veritas (DNV).
- [10] Det Norske Veritas (DNV E301) (2010). Offshore Standard Position mooring. <https://rules.dnvgl.com/docs/pdf/dnvgl/os/2015-07/dnvgl-os-e301.pdf>, Det Norske Veritas (DNV).
- [11] France Energie Marine (FEM) (2019). OMDYN2. <https://www.france-energies-marines.org/r-d/>.
- [12] Gao, W., Nelias, D., Lyu, Y., and Boisson, N. (2018). Numerical investigations on drag coefficient of circular cylinder with two free ends in roller bearings. *Tribology International*, 123:43–49.
- [13] Garrison, C. J. (1990). Drag and inertia forces on circular cylinders in harmonic flow. *Journal of Waterway, Port, Coastal, and Ocean Engineering*, 116(2):169–190.
- [14] Gaurier, B., Germain, G., Facq, J., Baudet, L., Birades, M., and Schoefs, F. (2014). Marine growth effects on the hydrodynamical behaviour of circular structures. *Proceedings of the 14th Journées de l'Hydrodynamique, Val de Reuil, France*.

- [15] Gaurier, B., Germain, G., Facq, J. V., and Bacchetti, T. (2018). Wave and current flume tank of ifremer at boulogne-sur-mer. description of the facility and its equipment.
- [16] Henry, P., Nedrebo, E., and Myrhaug, D. (2016). Visualisation of the effect of different types of marine growth on cylinders' wake structure in low re steady flows. *Ocean Engineering*, 115:182–188.
- [17] Jusoh, I. and Wolfram, J. (1996). Effects of marine growth and hydrodynamic loading on offshore structures. *Jurnal Mekanikal*, 1(1):77–86.
- [18] Marty, A., Berhault, C., Damblans, G., Facq, J. V., Gaurier, B., Germain, G., Soulard, T., and Schoefs, F. (2020a). Marine growth effect on the hydrodynamical behavior of a submarine cable under current and wave conditions. *Proceedings of 17èmes Journées de l'Hydrodynamique*.
- [19] Marty, A., Damblans, G., Facq, J. V., Gaurier, B., Germain, G., Germain, N., Harris, J., Maison, A., Peyrard, C., and Relun, N. (2020b). Experimental investigation of the seabed roughness effect on the hydrodynamical behavior of a submarine cable under current and wave conditions. *Proceedings of 17èmes Journées de l'Hydrodynamique*.
- [20] Marty, A., Germain, G., Facq, J. V., Gaurier, B., and Bacchetti, T. (2020c). *Experimental investigation of the marine growth effect on the hydrodynamical behavior of a submarine cable under current and wave conditions*. SEANOE, IFREMER <https://doi.org/10.17882/75373>.
- [21] Marty, A., Schoefs, F., Soulard, T., Berhault, C., Damblans, G., Facq, J. V., Gaurier, B., and Germain, G. (2021). Effect of roughness of mussels on cylinder forces from a realistic shape modelling. *Journal of Marine Science and Engineering - Ocean Engineering*, Under review.
- [22] Melbourne, W. H. and Blackburn, H. M. (1996). The effect of free-stream turbulence on sectional lift forces on a circular cylinder. *J. Fluid. Mech.*, 11:267–292.
- [23] Moe, G. and Gudmestad, O. T. (1998). Predictions of morison-type forces in irregular waves at high reynolds number. *International Journal of Offshore and Polar Engineering*, 8(4):273–279.
- [24] Morison, J. R., O'Brien, M. P., Johnson, J. W., and Schaaf, S. A. (1950). The forces exerted by surface waves on piles. *Journal of Petroleum Technology*, 2(5):149–154.
- [25] Mouslim, H., Babarit, A., Clement, A., and Borgarino, B. (2009). Development of the french wave energy test site sem-rev. *Proceedings of the 8th European Wave and Tidal Energy Conference, Uppsala, Sweden*.
- [26] O'Byrne, M., Pakrashi, V., Schoefs, F., and Ghosh, B. (2018a). Semantic segmentation of underwater imagery using deep networks. *Journal of Marine Science and Engineering - Ocean Engineering*, 6(3):93.
- [27] O'Byrne, M., Pakrashi, V., Schoefs, F., and Ghosh, B. (2020). Applications of virtual data in subsea inspections. *Journal of Marine Science and Engineering - Ocean Engineering*, 8(5):328.
- [28] O'Byrne, M., Schoefs, F., Pakrashi, V., and Ghosh, B. (2017). An underwater lighting and turbidity image repository for analysing the performance of image based non-destructive techniques. *Structure and Infrastructure Engineering - Maintenance, Management, Life-Cycle Design and Performance*, 14(1):104–123.
- [29] O'Byrne, M., Schoefs, F., Pakrashi, V., and Ghosh, B. (2018b). Stereo-matching technique for recovering 3d information from underwater inspection imagery. *Computer Aided Civil And Infrastructure Engineering*, 33(3):193–208.
- [30] Okamoto, T. and Yagita, M. (1973). The experimental investigation on the flow past a circular cylinder of finite length placed normal to the plane surface in a uniform stream. *Bulletin of Japan Society of Mechanical Engineers*, 16:805–814.

- [31] Picken, G. B. (1985). Review of marine fouling organisms in the north sea on offshore structures. *Discussion Forum and Exhibition on Offshore Engineering with Elastomers*, 5:5.1–5.10.
- [32] Sarpkaya, T. (1976a). In-line and transverse forces on cylinders in oscillatory flow at high reynolds numbers. *Journal of Ship Research*, 21(4):200–216.
- [33] Sarpkaya, T. (1976b). Vortex shedding and resistance in harmonic flow about smooth and rough circular cylinders at high reynolds numbers. Technical report, Naval postgraduate school, Monterey CA.
- [34] Sarpkaya, T. (1981). Moirison's equation and the wave forces on offshore structures. Technical report, Naval Civil Engineering Laboratory, Carmel CA.
- [35] Sarpkaya, T. (1985). In-line force on a cylinder translating in oscillatory flow. *Applied Ocean Research*, 7(4):188–196.
- [36] Schlichting, H. (1979). *Boundary layer theory*. McGraw-Hill book compagy, New York.
- [37] Schoefs, F., O'Byrne, M., Pakrashi, V., Ghosh, B., Oumouni, M., Soulard, T., and Reynaud, T. (2021). Feature-driven modelling and non-destructive assessment of hard marine growth roughness from underwater image processing. *Journal of Marine Science and Engineering*, Under review.
- [38] Spraul, C., Pham, H. D., Arnal, V., and Reynaud, M. (2017). Effect of marine growth on floating wind turbines-mooring lines responses. *23ème Congrès Français de Mécanique Lille*.
- [39] Teng, C. C. and Nath, J. H. (1989). Hydrodynamic forces on roughened horizontal cylinders. *21st Offshore Technology Conferencen Houston, Texas*.
- [40] Theophanatos, A. (1988). *Marine growth and hydrodynamic loading of offshore structures*. PhD thesis, University of Strathclyde, Glasgow (UK).
- [41] Theophanatos, A. and Wolfram, J. (1989). Hydradynamic loading on macro-roughened cylinders of various aspect ratios. *Journal of Offshore Mechanics and Arctic Engineering*, 111(3):214–222.
- [42] Vanhinsberg, N. P. (2015). The reynolds number dependency of the steady and unsteady loading on a slightly rough circular cylinder: From subcritical up to high transcritical flow state. *Journal of Fluids and Structures*, 55:526–539.
- [43] Verley, R. L. P. (1980). *Oscillations of cylinders in waves and currents*. PhD thesis, Loughborough University of Technology.
- [44] Xiaojie, T., Daoxi, L., Yingchun, X., Wei, D., and Dashuai, X. (2019). Experimental study on the hydrodynamic characteristics of cylinder with rough surface. *Journal of Marine Science and Technology*, 25:842–848.
- [45] Yang, S. H., Ringsberg, J., and Johnson, E. (2016). The influence of biofouling on power capture and the fatigue life of mooring lines and power cables used in wave energy converters. *Proc. Of the 2nd int. Conf, on Renew. Energies Offshore, Lisbon, Portugal*, pages 711–722.